Accepted Manuscript

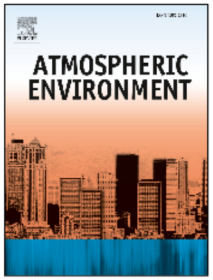

Vertical variability of aerosol single-scattering albedo and equivalent black carbon concentration based on in-situ and remote sensing techniques during the iAREA campaigns in Ny-Ålesund

K.M. Markowicz, C. Ritter, J. Lisok, P. Makuch, I.S. Stachlewska, D. Cappelletti, M. Mazzola, M.T. Chilinski

PII: S1352-2310(17)30395-3

DOI: 10.1016/j.atmosenv.2017.06.014

Reference: AEA 15376

To appear in: *Atmospheric Environment*

Received Date: 24 November 2016

Revised Date: 10 May 2017

Accepted Date: 6 June 2017

Please cite this article as: Markowicz, K.M., Ritter, C., Lisok, J., Makuch, P., Stachlewska, I.S., Cappelletti, D., Mazzola, M., Chilinski, M.T., Vertical variability of aerosol single-scattering albedo and equivalent black carbon concentration based on in-situ and remote sensing techniques during the iAREA campaigns in Ny-Ålesund, Atmospheric Environment (2017), doi: 10.1016/j.atmosenv.2017.06.014.

Vertical variability of aerosol single-scattering albedo and equivalent black carbon concentration based on in-situ and remote sensing techniques during the iAREA campaigns in Ny-Ålesund.

K.M. Markowicz[1], C. Ritter[2], J. Lisok[1], P. Makuch[3], I.S. Stachlewska[1], D. Cappelletti[4,5], M. Mazzola[5], M.T. Chilinski[1]

[1]Institute of Geophysics, Faculty of Physics, University of Warsaw, Warsaw, 02-093, Poland

[2]Alfred Wegener Institute, Helmholtz Centre for Polar and Marine Research, Potsdam, 14473, Germany

[3]Institute of Oceanology, Polish Academy of Sciences, Sopot, 81-712, Poland

[4]Department of Chemistry, Biology, and Biochemistry - University of Perugia, Perugia, I-06123, Italy

[5]National Research Council of Italy, Institute of Atmospheric Sciences and Climate, Bologna, 40129, Italy

Corresponding author: Krzysztof Markowicz (kmark@igf.fuw.edu.pl)

Highlights

- a new methodology to retrieve profiles of single-scattering albedo
- reasonable agreement between Raman and Klett retrievals
- small variability of single-scattering albedo with altitude over Svalbard
- slight increase in mean equivalent black carbon concentration with altitude

Abstract

This work presents a methodology for obtaining vertical profiles of aerosol single scattering properties based on a combination of different measurement techniques. The presented data were obtained under the iAREA (Impact of absorbing aerosols on radiative forcing in the European Arctic) campaigns conducted in Ny-Ålesund (Spitsbergen) during the spring

profiles of single scattering albedo (SSA) as well as absorption, extinction, and aerosol number concentration. Results have been obtained in an altitude range from about 400 m up to 1600 m a.s.l. and for cases with increased aerosol load during the Arctic haze seasons of 2015 and 2016. The main results consist of the observation of increasing values of equivalent black carbon (EBC) and absorption coefficient with altitude, and the opposite trend for aerosol concentration for particles larger than 0.3 μm. SSA was retrieved with the use of lidar Raman and Klett algorithms for both 532 and 880 nm wavelengths. In most profiles, SSA shows relatively high temporal and altitude variability. Vertical variability of SSA computed from both methods is consistent; however, some discrepancy is related to Raman retrieval uncertainty and absorption coefficient estimation from AE-51. Typically, very low EBC concentration in Ny-Ålesund leads to large error in the absorbing coefficient. However, SSA uncertainty for both Raman and Klett algorithms seems to be reasonable, e.g. SSA of 0.98 and 0.95 relate to an error of ±0.01 and ±0.025, respectively.

Keywords: aerosol, single-scattering albedo, black carbon, micro-aethalometer, lidar, arctic haze,

The climate impact of black carbon (BC) particles originating from fossil fuel combustion or biomass burning as well as mineral dust and volcanic ash is still very poorly understood, leading to scientific gaps relating to their role in the climate system (IPCC, 2013). These uncertainties are mainly due to the lack of vertical distribution of BC and the simplified description of the physical processes involving BC used for climate and aerosol modelling (Koch and Del Genio, 2010; IPCC, 2013). BC is reported as the second most important anthropogenic climate forcing agent (Ramanathan and Carmichael, 2008; Bond et al., 2013). The average top of the atmosphere (TOA) direct RF was estimated by many authors, ranging between 0.08 and 1.4 W/m^2 (Samset et al., 2013; Ramanathan and Carmichael, 2008; Bond, 2013). Such discrepancies of reported RF are mainly due to uncertainty related to vertical distribution of BC concentration (Samset et al., 2013). Regarding the extensive result overview of Samset et al., 2013 and Zarzycki and Bond, 2010, there is a strong need to develop efficient methodology for continuous monitoring of the vertical profiles of single scattering properties of aerosols on a global and regional scale, which would improve the knowledge on their climate impact.

The main motivation for this study is a deficiency of BC profile measurements in the Arctic, where the absorbing aerosol leads to strong positive TOA radiative forcing. In addition, the sensitivity study of BC concentration impact on the radiative budget shows high efficiency (Samset et al., 2013). Numerical simulation under a global aerosol model intercomparison project (AeroCom) (Myhre et al., 2013) shows that the BC columnar burden in the Arctic is 0.10±0.09 mg/m^2 while the mean global value is 0.19±0.06 mg/m^2 (Samset et al., 2013). Radiative forcing of BC in the Arctic is singly higher (0.38 ±0.30 W/m^2 in comparison to the global mean 0.36 ±0.16 W/m^2). The radiative forcing efficiency (forcing per BC unit of columnar concentration) over the Arctic (3792 ±328 W/g) is about two times larger than the global mean (1817 ±288 W/g) (Samset et al., 2013). According to Samset et al. (2013) BC particles above 5 km contribute to 72±15% to the radiative forcing. Such a high value for Arctic region is due to long-range transport in the middle and higher troposphere from Asia, Europe, and North America. The vertical distribution of absorbing aerosols is

There are a limited number of observations of BC and aerosol absorption in the Arctic. Observation of direct and diffuse spectral solar radiation within the AERONET network (Holben et al., 1998) can be used to retrieve the single scattering albedo (SSA) and absorbing optical depth. However, the uncertainty is high in the case of clean air mass. Dubovik et al. (2002) reported that SSA can be retrieved with an accuracy of about ±0.03 when the aerosol optical depth (AOD) at 440 nm reaches at least 0.4 for a solar zenith angle higher than 50^{o}. In the case of Arctic conditions such a high AOD is observed very rarely (Pakszys et al., 2015), so retrieval of SSA and absorbing AOD has little meaning. In-situ observation of aerosol absorption delivers more precision data for a few Arctic stations. In the Ny-Ålesund (Spitsbergen), Barrow (Alaska), Alert (Canada), and Summit (Greenland) stations the equivalent black carbon (EBC) concentration (Petzold et al., 2013) as well as the aerosol absorption is measured by Particle-Soot Absorption Photometers (PSAP) or Aethalometers (Stohl et al., 2006). In addition, combined measurement with nephelometers allows the estimation of the SSA. However, such observations provided the data only for the surface layer. In Ny-Ålesund the station at Zeppelin Mountain (460 m a.s.l.) can be used to estimate some vertical variability of absorbing aerosol properties. The active remote sensing observation by the lidar system has little potential to retrieve the profiles of SSA or absorbing coefficient. Theoretically, a multichannel elastic and Raman lidar system can be used to estimate such parameters, but the uncertainty of the indirect method is usually high. The uncertainty of the data inversion products is the combination of errors introduced by the inversion procedure itself and uncertainties on optical input parameters such as backscattering and extinction coefficient (Noh, 2014). The vertically resolved aerosol absorption coefficient and SSA were retrieved using the inversion algorithm by many authors (e.g. Müller et al., 1999; Veselovskii et al., 2002; Veselovskii et al., 2004; Kolgotin and Müller, 2008; Chaikovsky et al., 2016). Another possibility to obtain vertical variability of absorbing aerosol is atmospheric sounding. The micro-aethalometer AE-51 is often used onboard UAVs (Ramana et al., 2007; Chilinski et al., 2016) or tethered balloons (Ferrero et al., 2011; Mazzola et al., 2016; Ran et al., 2016). Such measurements were done in Ny-Ålesund in 2011 and 2012 by Ferrero et al., 2016. Based on about 200 vertical profiles measured during spring

The main objective of this paper is to investigate the aerosol light-absorbing characteristics over Svalbard, obtained from an AE-51 aethalometer onboard a tethered balloon together with lidar observations, in order to improve the retrieval of the single scattering albedo. Independent measurement of the aerosol extinction and absorbing profiles allowed us to avoid the limitation of indirect lidar retrievals. The next section is devoted to the description of the instrumentation and research stations. The methodology is discussed in the Section 3, while uncertainty analysis is given in Section 4. The cases under study include one period in 2015 and one in 2016 and are described in Section 5. Section 6 includes information about the profile of EBC and total aerosol number concentration. Finally, the summary and conclusion are presented in Section 7.

2. Description of research stations and equipment

During the iAREA (Impact of Absorbing aerosols on Radiative forcing in the European Arctic) campaigns in 2014, 2015, 2016, and 2017 aerosol measurements, both in-situ and remote sensing, were carried out in Ny-Ålesund (Fig. 1). The research village is located on the west coast of Spitsbergen in Kongsfjorden, surrounded by mountains from three sides and with the fiord opening in north-west direction. Aerosol in-situ observations were provided at the Gruvebadet observatory (78.918^{o}N, 11.895^{o}E, 61 m a.s.l) located 800 m south-west from Ny-Ålesund research village. The aerosol remote sensing observations and tethered balloon profiles were conducted at the French-German Arctic Research Base AWIPEV (Alfred Wegener Institute and Polar Institute Paul Emile Victor) (78.923^{o}N, 11.923^{o}E, 10 m a.s.l.) in Ny-Ålesund .

A 9 m^3 tethered balloon was equipped with a payload including Vaisala radiosonde sensors for temperature, relative humidity and pressure, and wind speed and direction, and aerosol in-situ devices. The aerosol absorption and EBC concentration was measured by a micro-aethalometer AE-51, while the aerosol number concentration was assessed by HandiLaz (in 2015) and OPC-N2 (in 2016).

The micro-aethalometer AE-51 measures the light transmission through a Teflon-coated glass fibre filter at 880 nm. A change in filter attenuation is then translated to the mass

was measured before and after every balloon launch. Each part of the experiment was held with the same integration time and flow mentioned above. During conducting profiles, results were automatically stored on a built-in logger. According to the manufacture's information, the resolution of measurements is 1 ng/m^3, while precision is ±100 ng/m^3 for one-minute averaging. The device's operational weight is approximately 280 grams. Ferrero et al. (ACP 2016) investigated the accuracy of the EBC measurement by AE-51 and found that 20 ng/m^3 can be considered the limit above which a single measurement is not affected by instrumental noise.

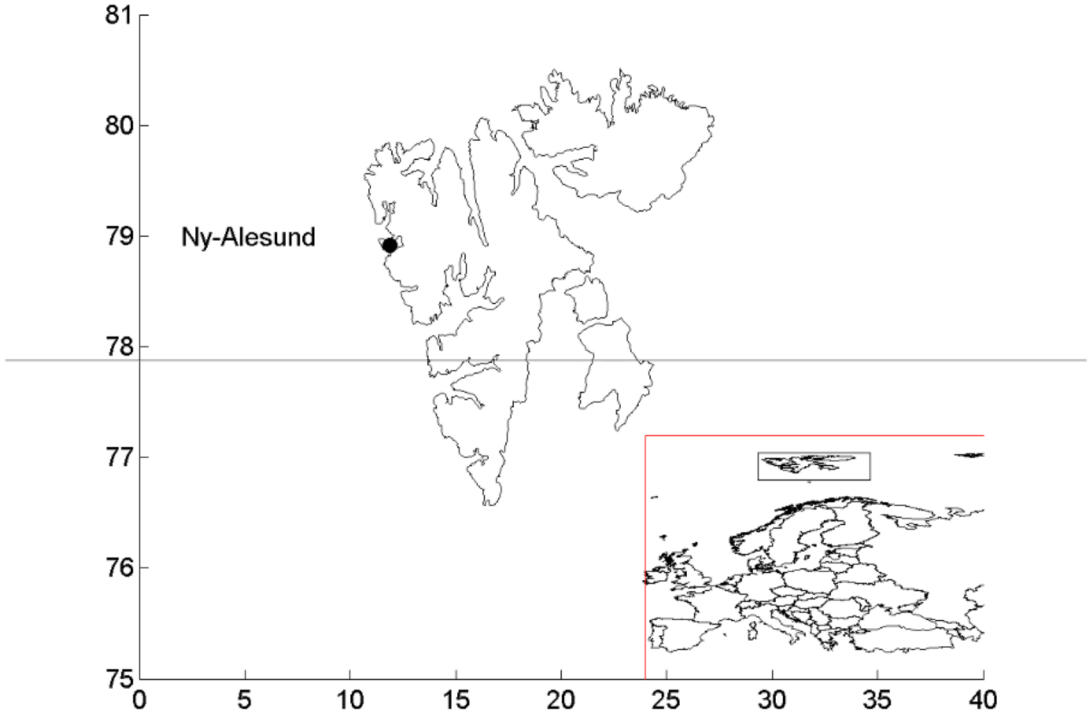

Fig. 1. Map of the Svalbard region.

The OPC-N2 optical counter from Alphasense measures the light scattered (658 nm) by individual particles carried in a sample air stream through a laser beam. These

185 part of the illuminating laser beam and ensure accurate sizing. The instrument classifies each
186 particle size at rates of up to ~10 000 particles per second, recording the particle size to one of
187 16 bins covering the size range from 0.38 to 17 µm. The flow rate is about 220 ml/min. The
188 data are transmitted via an SPI to a Raspberry Pi microcomputer every one second.
189 A HandiLaz particle counter was used to measure profiles of the aerosol number
190 concentration during the campaign in 2015. This handheld laser-based device includes four
191 channels (thresholds 0.3, 0.5, 1.0, and 5.0 µm). The aerosol can be sampled with 10-second
192 resolution under a stabilised flow rate of 2.3 l/min.
193
194 Table 1. Instruments used for studies of aerosol optical properties during the iAREA
195 campaigns in Ny-Ålesund

Ground-based Instrument	Acronym	Wavelength [nm]; Range, Size [nm]	Quantities	Year	Station
AWI Aerosol Raman Lidar KARL	KARL	355, 387, 532, 607, 1064	extinction, backscatter coefficient	2015 2016	Ny-Ålesund
AWI Sun photometer SP1A	SP1A	369, 381, 413, 500, 610, 674, 779, 860, 945, 1023	aerosol optical depth, Angstrom exponent, precipitable water	2015 2016	Ny-Ålesund
Microtops II Sun Photometer	MII	440, 500, 675, 870, 1020	aerosol optical depth, Angstrom exponent	2015 2016 2017	Ny-Ålesund
micro-Aethalometer	AE-51	880	equivalent black carbon concentration	2015 2016 2017	Ny-Ålesund (Balloon)
Aethalometer	AE-31	370, 450, 571, 615, 660, 880, 950	absorption coefficient, equivalent black carbon concentration	2014 2015 2016 2017	Gruvebadet

					(Balloon)
Photoacoustics extinctiometer	PAX	532, 870	Absorption coefficient, scattering coefficient	2016 2017	Laboratory work, calibration

196

197 The KARL Raman lidar (Tab. 1) measures the backscatter coefficient at 355, 532, and
198 1064 nm, extinction coefficient and depolarisation at 355 and 532 nm, as well as water vapour
199 at 407 and 660 nm. This lidar is a coaxial system with a 50-Hz Nd:Yag laser, which emits
200 about 10 W for each of the three wavelengths. It consists of a 70-cm detection mirror working
201 at an field of view of approximately 2 mrad. An aperture top that is movable in position and
202 diameter allows measurements in the troposphere (overlap range above 700 m) and
203 stratosphere. The technical parameters and data analysis techniques have been described by
204 Hoffmann (2011) and Ritter et al., (2016). The uncertainties in the aerosol backscatter
205 coefficient retrieval at 355 nm and 532 nm are up to 5% and 10%, respectively, at 1064 nm,
206 while the error for the aerosol extinction coefficient at 355 nm is up to 50% and at 532 nm is
207 up to 100% at 4 km altitude (Ritter et al., 2016). Below 700 m altitude the backscatter and
208 extinction profiles can be retrieved by comparing the KARL lidar with a Vaisala CL51
209 ceilometer on site. During clear and stable meteorological conditions data from the ceilometer
210 operating at 910 nm is evaluated with a boundary above 700 m and with values derived by
211 KARL lidar. Under the assumption that the wavelength dependence of backscatter and
212 extinction as derived by KARL lidar is also valid in the boundary layer and that all deviations
213 in the results between ceilometer and KARL are only due to the incomplete overlap of the
214 latter instrument, this overlap can be corrected.

215 AOD and Angstrom exponent (AE) were provided by a Full-Automatic Sun
216 Photometer SP1A (Tab. 1) produced by Dr. Schulz and Partner GmbH
217 (http://www.drschulz.com/cnt/) and by Microtops II sun photometer. The SP1A sun
218 photometer measures direct solar radiation in 10 channels between 369 nm and 1023 nm with
219 a field of view of 1˚ (Herber et al., 2002). The measured signal is temperature corrected
220 within a limit of -30^{o}C to 40^{o}C. Langley methodology for the instrument calibration is

minute "shots" in which measurements were made at all wavelengths, 10 seconds per channel: 440, 500, 675, 870, and 1020 nm. Further technical parameters and calibration techniques have been described by Morys et al., 2001 and Markowicz et al., 2012.

Aerosol scattering properties were measured by nephelometer 3563 from TSI operating on three wavelengths with one-minute resolution (Anderson et al., 1996). The data from the nephelometer was corrected for angular non-Lambertian illumination and truncation errors based on the methodology described by Anderson et al., 1996 and Anderson and Ogren, 1998. The uncertainty of the aerosol scattering coefficient due to both effects is about 3% for a single scattering albedo larger than 0.8. For very low single scattering albedo the errors are much higher and reach about 30% at a single scattering albedo of 0.4 (Massoli at al., 2009). Several previous studies have estimated the total uncertainty in the scattering coefficient measured by TSI nephelometer at somewhere around 10% (Heintzenberg et al., 2006).

A Magee aethalometer AE-31 was used to measure the EBC concentration at Zeppelin station and Gruvebadet laboratory. The aethalometer measures the transmission through a quartz filter over a wide spectrum of wavelengths, in our case between 370 and 950 nm. EBC concentration is then calculated via the derivative of attenuation. In the case of AE-31 instruments the data must be corrected for filter non-linear loading effects and multiple scattering, which leads to enhancement of light absorption by particles in the filter matrix. For this purpose, we use the methodology described by Segura et al., 2014. The uncertainty of the EBC concentration is about 8% (Eleftheriadis et al., 2009).

One wavelength Photoacoustic Extinctiometer (PAX) is an instrument from the Droplet Measurement Technologies company, measuring scattering and absorption coefficients as well as the single scattering albedo (SSA) and EBC mass concentration (Kok et al., 2010). It uses photoacoustic methods to retrieve absorption by detection of pressure waves initiated by the heat release due to the absorption of laser light. The construction of the scattering chamber is based on the nephelometer technique. The detection limit for one-minute averaging for the absorption and scattering coefficient is less than 0.25 Mm^{-1} (870 nm). The detector measures scattering light between 6 and 174^{o}. PAXs at 532 and 870 nm are used in the Laboratory of the Institute of Geophysics in Warsaw (Poland) to estimate the

coefficient by the lidar techniques are almost impossible, additional information about the profile of this quantity can improve the single scattering albedo vertical distribution estimation. The AE-51 micro-aethalometer reports the EBC concentration deposited on the quartz filter, which can be used to estimate the aerosol absorption coefficients. However, computation of the EBC concentration aerosol absorption coefficient is complicated due to light multiple scattering between the filter and the aerosol layer (see below).

In addition, the data obtained from micro-aethalometer device includes non-realistic negative values when sampling is performed in clear conditions or at a high time-resolution. In such cases the attenuation (ATN) values may remain unchanged or may even decline slightly between time steps due to the instrumental noise. In order to limit this effect, filter methods can be exploited to reduce the signal-to-noise ratio. The first step is the averaging of the ATN signal before the signal derivative. To do this we use a run mean filter with a time window of 100 seconds, which corresponds to vertical averaging of about 130 m. Fluctuation of EBC concentration due to electronic noise was estimated thanks to a comparison of two identical AE-51 instruments. Figure 1 shows the root mean square error (RMSE) and standard deviation (STD) of EBC difference as a function of the time averaging. In the case of the one-second data (without smoothing) the RMSE and STD are very large (above 1000 ng/m^3). Once the time averaging window is increased, both parameters decrease significantly. For example, for a 100-second average the RMSE reaches about 65 ng/m^3, while for a 10-minute average it declines to about 55 ng/m^3.

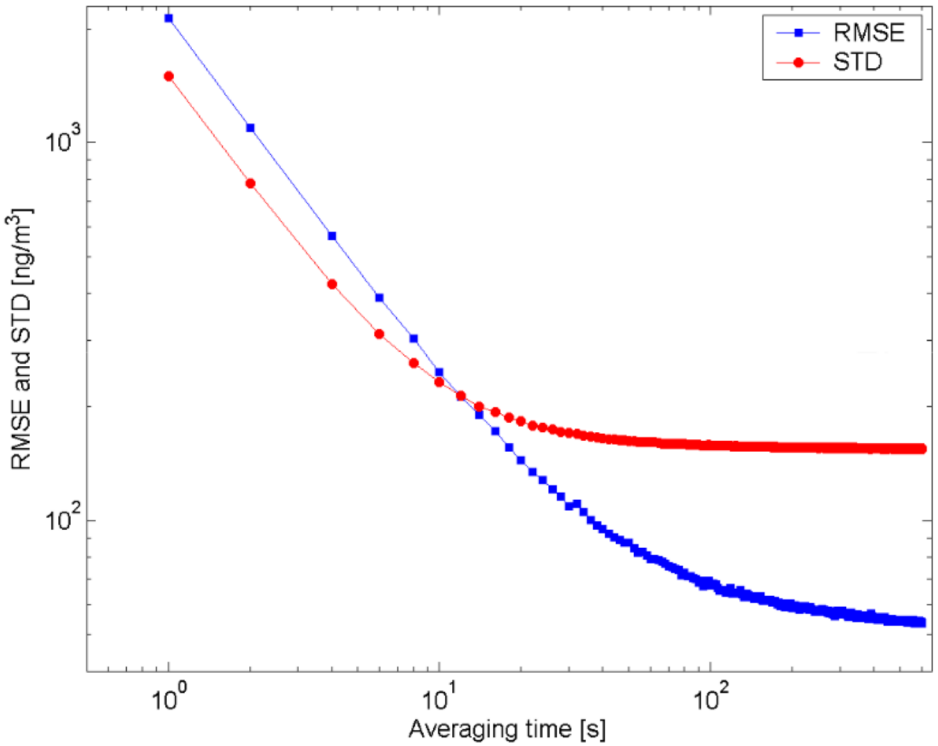

Fig. 2. The root mean square error (blue line) and standard deviation (red line) of the EBC concentration difference between two AE-51 aethalometers as a function of averaging time [s].

These values correspond to the RMSE for absorption coefficients of 0.33 Mm^{-1} and 0.28 Mm^{-1}, respectively.

After reduction of ATN noise the aerosol absorbing coefficient (σ_{ABS}) and EBC concentration are computed from the ATN derivative

$$\sigma_{ABS} = \frac{dATN}{dt}\frac{A}{Q \cdot C \cdot R(ATN)} \quad (1)$$

$$EBC = \frac{dATN}{dt}\frac{A}{Q\sigma_{ATN}} \quad (2)$$

where A is a sample spot area ($7.1 \cdot 10^{-6}$ m^2), Q is the volumetric flow rate, C is the multiple

297 higher than 20. Therefore, we changed the filter every time ATN exceeded the threshold
298 value. Taking into account the multiple scattering effects is not straightforward because
299 enhancement of light attenuation depends on several aerosol and filter optical parameters.
300 Previous studies including AE-31 aethalometer measurements show different approaches to
301 correct the aerosol absorption coefficient (Schmid et al., 2006; Collaud-Coen et al., 2010;
302 Rizzo et al., 2011; Segura et al., 2014; Virkkula et al., 2015). In the case of the AE-51 a
303 multiple scattering optical enhancement factor of 2.05±0.03 was estimated by Ferrero et al.,
304 2011. A higher value (2.98±0.05) has been assumed by Ran et al., 2016 based on the MAAP
305 (Multi-angle absorption photometer) and AE-31 aethalometer. In the present study the C
306 factor has been estimated with a comparison of experiment versus the PAX (870 nm) device,
307 between 30 March and 4 April 2017 in Ny-Alesund (Fig. 3).
308
309 Table 2. The scattering optical enhancement factor obtained during field experiments

Year	**Region**	**C value**	**references**
2014	China	2.98±0.05	Ram et al., 2016
2008	Italy	2.05±0.03	Ferrero et al., 2011
2015	Poland	5.54±0.05	Chilinski et al., 2017
2017	Arctic	2.75±0.10	this study

310
311 The scattering optical enhancement factor obtained in this comparison is 2.75±0.10, slightly
312 higher than that reported by Ferrero et al., 2011 in Italy and lower than that reported by Ran et
313 al., 2016 in China. In the present study, we determined also the multiple scattering factor for
314 AE-31 (2.88±0.08) and found it to be slightly lower than that obtained by Schmid et al., 2006;
315 Collaud-Coen et al., 2010; and Segura et al., 2014. Figure 2 shows the comparison of the 60-
316 minute average of the aerosol absorption coefficient from AE-51 and PAX after applying the
317 new multiple scattering factor to Equation 1. The agreement is highly satisfactory with a
318 correlation coefficient (r^2) of 0.64, a root mean square error of 0.12 Mm^{-1}, and a mean bias of
319 0.01 Mm^{-1}. Comparison of EBC concentrations recorded simultaneously by AE-31 and AE-51

hPa pressure and 25°C air temperature), possible thanks to a new flow speed meter based on air mass measurements decaying with altitude (Chilinski et al., 2016).

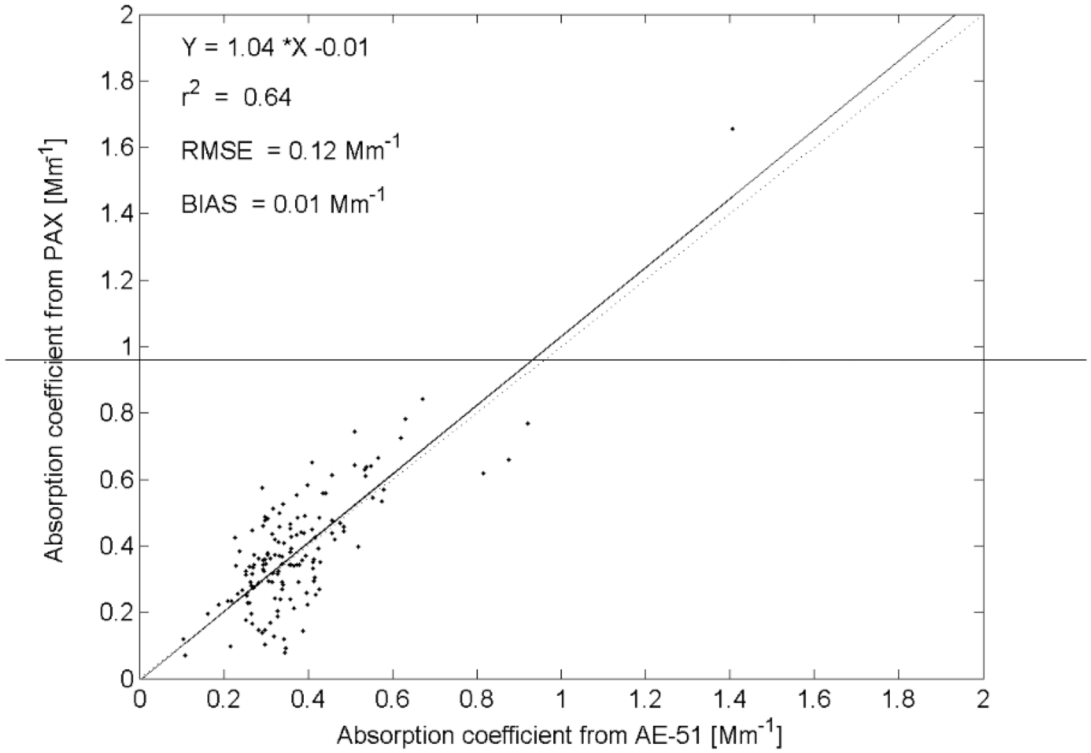

Fig. 3. Comparison of the absorption coefficient obtained from AE-51 aethalometer at 880 nm and PAX at 870 nm after taking into account the multiple scattering effects in the AE-51. Both PAX and AE-51 data are averaged to 60-minute intervals.

Profiles of SSA were computed, yielding

$$SSA = 1 - \frac{\sigma_{ABS}}{\sigma} \quad (3)$$

where σ is the aerosol extinction coefficient. Due to the different wavelength of the AE-51, KARL lidar, either the aerosol absorption coefficient at 880 nm needed to be converted to 532 nm or the extinction coefficient should be converted to 880 nm. For the two conversions, we used two different methods for SSA estimation. In the first method we applied Raman

to values characteristic for soot particles (Russell et al., 2010). Although the AAE variability might be significant (Russell et al., 2010; Schuster et al., 2016), its impact on the SSA uncertainty is small in comparison to other variables (see Section 4). The extinction coefficient at 532 nm is retrieved directly from 532 and 607 Raman channels, while the absorption coefficient at 880 nm is calculated using the EAE (extinction Angstrom exponent) defined for the extinction coefficient at 355 and 532 nm. This approach assumes the vertical variability of the EAE to be constant with wavelength; however, previous studies show that columnar EAE (averaged in the whole atmospheric column) can change with wavelength due to variability of aerosol size distribution (O'Neill et al., 2003; Soni et al., 2011; Kaskaoutis et al., 2007). Therefore, sun photometer observations of AE are used to scale the profile EAE estimated from lidar observations. The modified profile of $EAE_n(z)$ is defined from

$$EAE_n(z) = EAE(z)\frac{AE}{\int EAE(z)dz} \quad (4)$$

Also, due to significant noise of the lidar's retrieved EAE, the vertical profiles were averaged by means of run mean filter with a window resolution of 375 m. This method hereinafter will be referred to as the "Raman method".

In the second method the extinction coefficient at 532 nm is directly computed from the backscattering coefficient at 532 nm. The extinction coefficient at 880 nm, however, is computed as a value normalised by the AOD(τ) of the backscattering coefficient at 880 nm, which in turn is estimated from the backscattering coefficient at 532 and 1064 nm by means of Angstrom logarithm interpolation. AOD(τ) measured by the sun photometer is related with the lidar extinction coefficient, yielding

$$\sigma(z) = \beta(z)\frac{\tau}{\int \beta(z)dz} \quad (5)$$

Normalisation of the backscattering coefficient corresponds to altitude invariance of the lidar ratio method (Klett, 1981). During cloudy conditions when AOD data were not available, we estimated the extinction coefficient using an assumed lidar ratio of 40 sr, which for visible wavelengths seems to be a reasonable choice for Arctic aerosols (Ritter et al., 2016). The

373 includes first the calculation of the extinction profile from the lidar profiles at the Raman
374 shifted wavelength. Next, the backscatter profile is obtained by the ratio of the elastic to
375 inelastic lidar profile. To retrieve the aerosol extinction and backscatter, the Rayleigh
376 contribution due to clear air is subtracted using the air density profile from the Vaisala RS-92.
377
378 **4. Uncertainty analysis**
379 SSA uncertainty is related to independent errors of the lidar's retrieval of the
380 extinction and absorption coefficients measured by the AE-51

381 $$\delta SSA = (1 - SSA)\sqrt{\left(\frac{\delta\sigma_{ABS}}{\sigma_{ABS}}\right)^2 + \left(\frac{\delta\sigma}{\sigma}\right)^2} \quad (6)$$

382 Extinction coefficient uncertainties mainly consist of:
383 - lidar electronic and Poisson noise
384 - background noise
385 - molecular scattering and extinction coefficients
386 - conversion of the extinction from 532 and 355 to 880 nm (Raman method)
387 - conversion of backscattering coefficient from 532 and 1064 to 880 nm and calculations of
388 backscattering to extinction coefficient (Klett method).
389 Due to the increase in lidar noise with altitude we have made uncertainty analysis in three
390 layers (0.5-1.0, 1.0-1.5, and 1.5-2.0 km). The uncertainty of aerosol extinction (532 nm)
391 retrieval from the Raman channel (607 nm) is 18, 21, and 40 % (Table 2), respectively, for the
392 first, second, and third layer. In the case of the SSA computed at 880 nm the extinction
393 coefficient must be converted to this wavelength. The main error is related to the EAE
394 computed from lidar extinction profiles at 355 and 532 nm and from AE retrieved from sun
395 photometer observations at 500 and 870 nm, which is used to scale the lidar EAE. Finally, for
396 the Raman method the uncertainties of extinction coefficient at 880 nm are 27, 34, and 58%,
397 respectively. The errors of the backscattering coefficient (Klett method) at 532 nm are 3, 3,
398 and 5%, respectively, while for 880 nm they are 6, 6, and 8%. For both backscattering
399 coefficients at 532 and 880 nm the conversion to extinction is needed. To estimate the

Table 3. Relative uncertainties for the aerosol extinction ($\delta\sigma/\sigma$) and backscattering ($\delta\beta/\beta$) coefficients for Raman and Klett methods at 532 and 880 nm. Data are averaged between 0.5 and 1.0 km, 1.0-1.5 km, and 1.5-2.0 km.

Layer levels [km]	Raman		Klett			
	$\delta\sigma/\sigma$ (λ=532)	$\delta\sigma/\sigma$ (λ=880)	$\delta\beta/\beta$ (λ=532)	$\delta\sigma/\sigma$ (λ=532)	$\delta\beta/\beta$ (λ=880)	$\delta\sigma/\sigma$ (λ=880)
0.5-1.0	±0.18	±0.24	±0.03	±0.20	±0.06	±0.21
1.0-1.5	±0.21	±0.31	±0.03	±0.20	±0.06	±0.21
1.5-2.0	±0.40	±0.53	±0.05	±0.21	±0.08	±0.22

Retrieval of absorption coefficient leads to errors related to:

- instrument electronic and optical noise,
- multiple scattering effect between filter and aerosol layer,
- uncertainties of flow meter measurements and conversion of the air density to standard conditions,
- conversion of the absorption coefficient from 880 to 532 nm.

In the case of the electronic and optical noise the fluctuation can be reduced by data averaging, while for multiple scattering effect and spectral absorption coefficient conversion the error depends mostly on the aerosol single scattering properties. Both effects are estimated during comparison with PAX instruments. The electronic and optical noise was obtained from two AE-51 device comparisons (Fig. 3). The RMSE of the EBC and absorption coefficient at one-minute resolution is 68 ng/m^2 and 0.34 Mm^{-1}, respectively. The RMSE between corrected AE-51 and PAX absorption coefficients is 0.12 Mm^{-1}. This value was obtained for hourly mean AE-51 and PAX data and therefore does not include the electronic and optical noise. Thus the value of ±0.12 Mm^{-1} corresponds to the uncertainty due to multiple scattering effect (Table 4). For the flow meter and air density correction the uncertainty is somewhat constant and was estimated at the level of 2%. To compute the error related to aerosol absorption

coefficient at 532 nm of 0.09 Mm^{-1}. This value corresponds to a relative uncertainty of about 12%.

Table 4. Uncertainty of the absorption measurements by the AE-51 micro-aethalometer

Parameter	Instrument noise at 1-minute resolution	Flow and air density	Multiple scattering effect	Conversion 880 to 532 nm	Total
Absorption	±0.35 Mm^{-1} ± 48%	±2%	±0.12 Mm^{-1} ±17%	±0.09 Mm^{-1} ±12%	±0.38 Mm^{-1} ±51%

Based on uncertainties for absorbing and extinction coefficients, we estimated the SSA error (Equation 6). Table 5 shows SSA uncertainties for the Raman and Klett methods at three different altitudes and for three selected SSA levels. Comparison of uncertainties of the Raman and Klett algorithms indicates negligible differences. Errors calculated for high SSA (0.98) are about ±0.01 at 532 nm and within the range ±0.01 to ±0.02 at 880 nm. In the case of a moderate load of absorbing aerosols (SSA=0.95) the uncertainties seem to be higher, varying between ±0.02 and ±0.03 for Raman and about ±0.02 for Klett methods at 532 nm. Regarding the SSA of 0.9, the calculated errors are significantly higher, up to 0.03–0.05, for both methods at 532 nm.

Table 5. Uncertainty of SSA for Raman and Klett methods defined for three altitude layers (0.5-1.0 km, 1.0-1.5 km, and 1.5-2.0 km) and for three selected SSA values (0.98, 0.95, and 0.9). SSA error is given for 532 nm and for 880 nm (value in parentheses).

SSA	Raman			Klett		
	0.5-1.0 km	1.0-1.5 km	1.5-2.0 km	0.5-1.0 km	1.0-1.5 km	1.5-2.0 km
0.98	±0.01 (±0.01)	±0.01 (± 0.01)	±0.01 (± 0.02)	±0.01 (±0.01)	±0.01 (± 0.01)	±0.01 (± 0.01)

Slightly higher error is found at 880 nm for both methods due to the previously described conversions of extinction coefficient to corresponding wavelengths. The increasing value of SSA uncertainties with altitude (especially for the third layer [1.5-2.0 km]) is related both with the lidar retrieval error and the significant decline of absorption coefficient with altitude. The significantly high uncertainties of SSA retrieval are mainly due to AE-51 noise related to the data sampling close to the instrument's detection limit in a pristine environment. Thus, while instrumental error is somewhat constant, using the algorithms for cases with higher particle concentrations would result in lower SSA uncertainties.

5. Case study

This section contains a detailed discussion of aerosol events observed during the springs of 2015 and 2016. We selected days with higher aerosol absorption coefficient, indicated by the long-range transport from middle-latitudes.

5.1. Aerosol event between 22 and 24 March 2016

In 2016 an anthropogenic event took place between 22 and 24 of March. Although the number of data is rather small due to cirrus cloud contamination, the AOD show values of about 0.08 (500 nm) on 21 March and between 0.11 and 0.14 on March 24, indicating higher concentrations of aerosols as measured by SP1a and Microtops II sun photometers. Furthermore, the NAAPS model (Fig. 4) indicates an advection of sulphates over the North Pole and Svalbard (orange and red colour) between 22 and 25 March. Modelled AOD at 550 nm reaches 0.2-0.4, a very high value for the Arctic, with no significant contribution of dust and smoke particles. The origin of the mass over Svalbard can be identified by the HYSPLIT (Draxler and Rolph, 2010) back trajectories (Fig. 5). The 144-hour back trajectories ending in Ny-Ålesund at 00 UTC on 22 (a), 23 (b), 24 (c), and 25 (d) March show the transport of air mass from the middle latitudes. Although the transport is significantly different between 1 and 5 km a.g.l, the HYSPLIT results indicate possible advection of air pollution from Siberia. Thus anthropogenic particles from middle latitudes, as well as the biomass burning from boreal forest, could be expected.

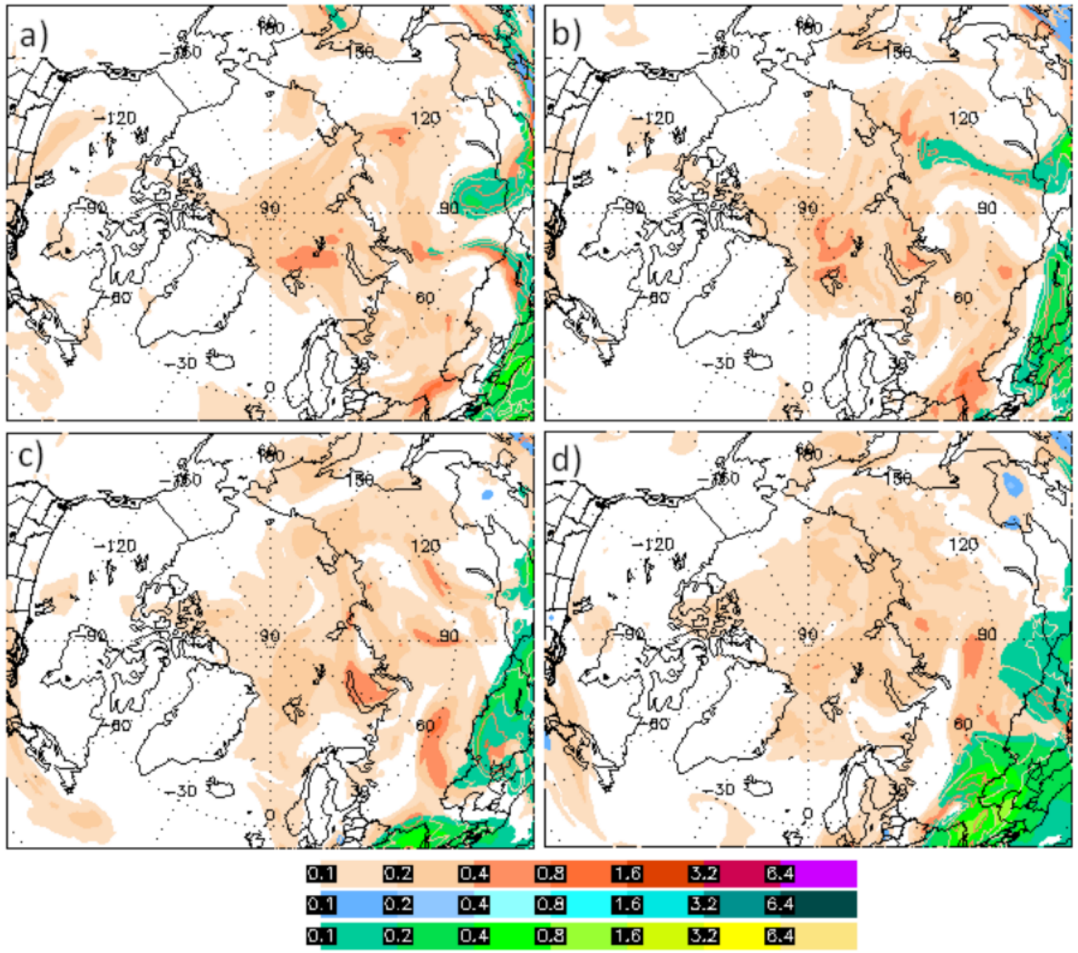

Fig. 4. NAAPS aerosol optical depth at 550 nm for 00 UTC on 22 (a), 23 (b), 24 (c), and 25 (d) March 2016. The orange/red colour corresponds to anthropogenic sulphates, blue to smoke particles, and green/yellow to dust. The colour bars for each aerosol component vary between 0.1 and 12.8.

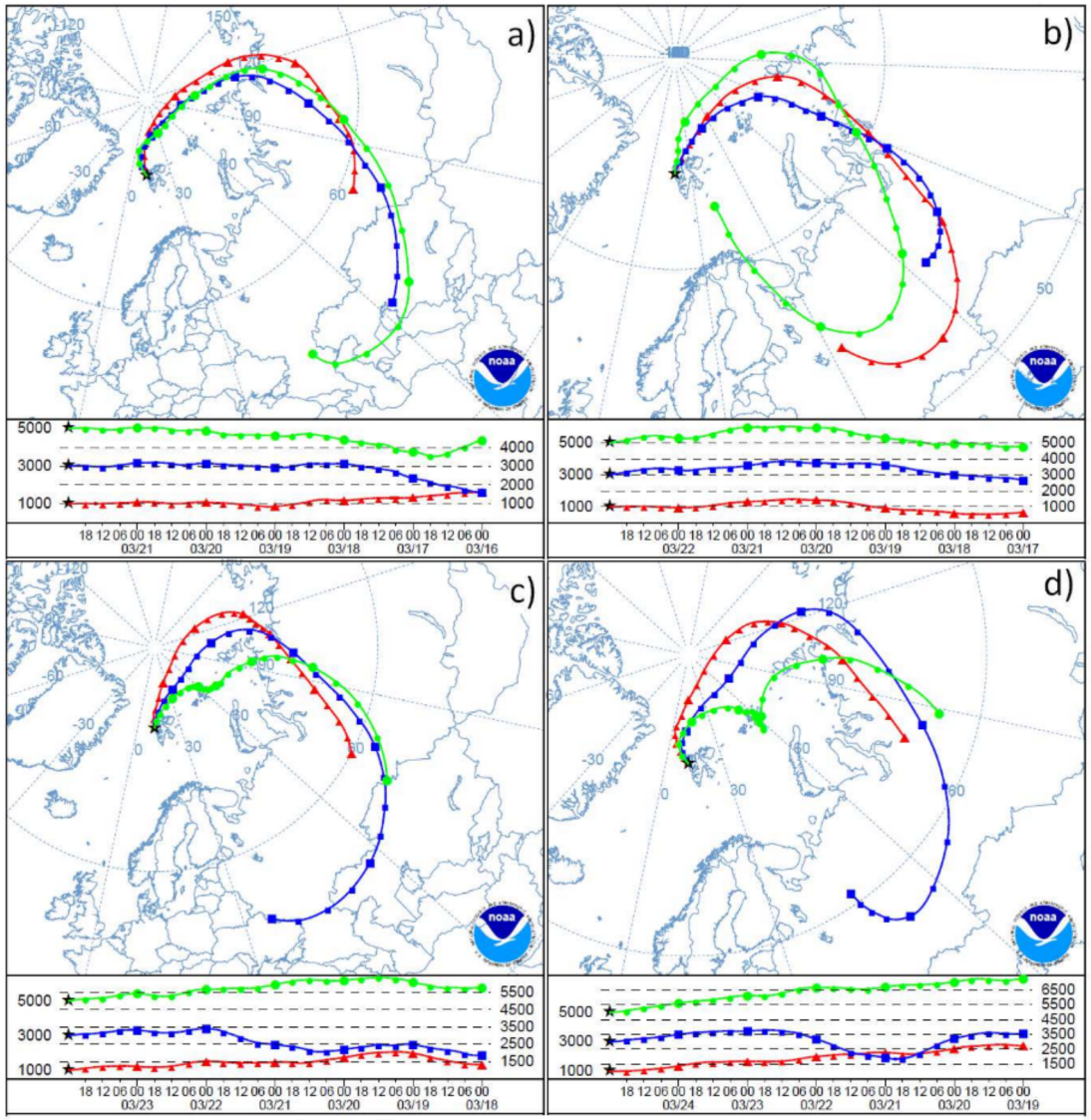

Fig. 5. 144-hour air mass back trajectories obtained from the NOAA HYSPLIT model at 00:00 UTC for 22 (a), 23 (b), 24(c), and 25 (d) March 2016. Panels a-d are generated by means of the NCEP reanalysis database for Ny-Ålesund at 1, 3, and 5 km.

During this event, four tethered balloon profiles were conducted. Figure 6 shows aerosol absorption coefficient and EBC concentration as a function of altitude. The blue and green lines show data for 23 March around 13:40 and 18:20 UTC, respectively. In these cases,

498 and also close to 1000 m and 1200-1400 m. EBC concentration and absorption coefficient
499 decrease with altitude. The maximum values of EBC concentration observed during this event
500 are significantly higher than the long-term mean (2005-2014) for spring season of 44 ng/m^3
501 measured by the AE-31 aethalometer at the Zeppelin station (460 m a.s.l.) (Lisok et al., 2016).

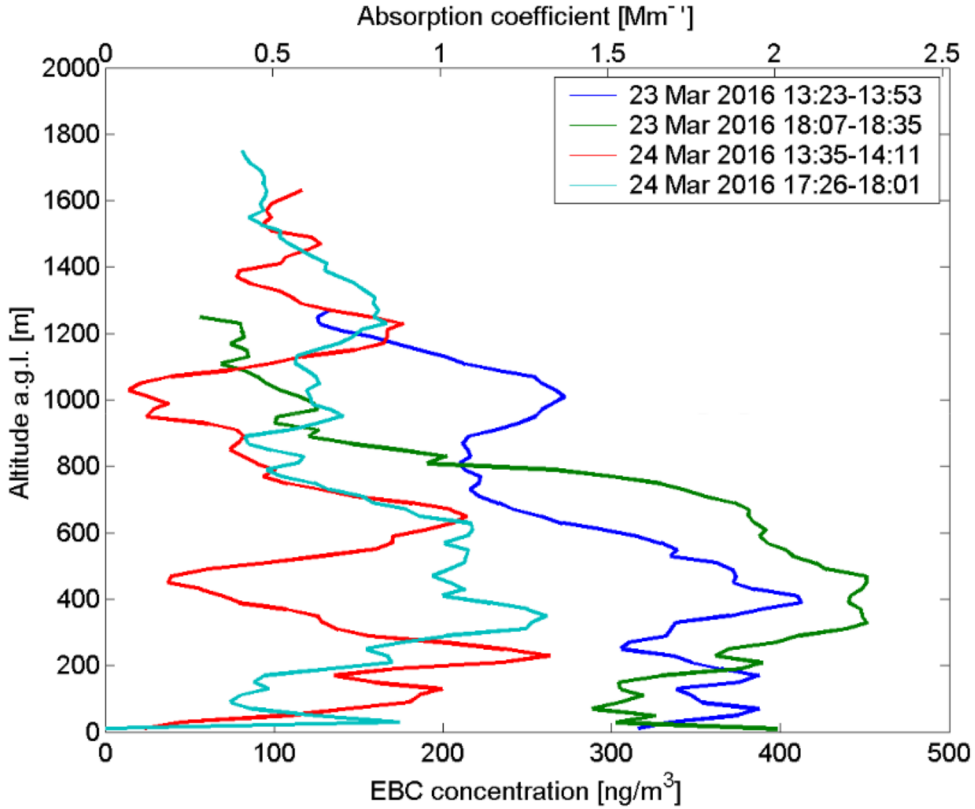

502
503

504 Fig. 6. Vertical variability of the EBC concentration and absorption coefficient at 880 nm
505 from AE-51 onboard the tethered balloon soundings made on 23 and 24 March 2016 between
506 13:23 and 13:53 UTC (blue line), 18:07-18:35 (green line), 13:35-14:11 (red line), and 17:26-
507 18:01 (grey line).
508

509 Due to cloud contamination only two KARL lidar profiles were retrieved in a close
510 time period with balloon soundings on 23 March. Figure 7 shows profiles of (a) SSA, (b)
511 extinction, and (c) absorption coefficients from profiles obtained between 13:35 and 14:11

600 and 1200 m. Vertical variability of the SSA profiles is significant but similar for Raman and Klett algorithms. Also, the Raman method indicates negligible dependency with respect to wavelength and, at some altitudes, Raman and Klett retrievals reveal appreciable dissimilarities. Extinction coefficient calculations are believed to be responsible for the discrepancy, as shown at the layer around 1.2 km, where Raman SSA is significantly lower (Fig. 7b). Evening profiles show similar

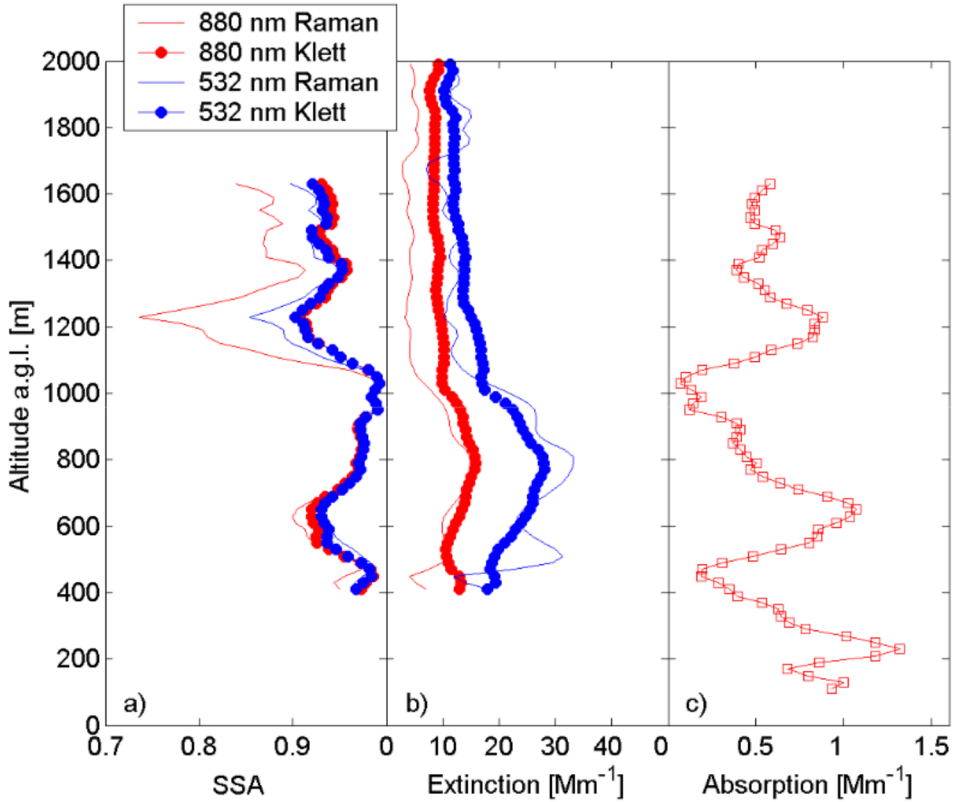

Fig. 7 Profiles of SSA (a), extinction coefficient (b), and absorption coefficient at 880 nm (c) in Mm^{-1} obtained during the tethered balloon and KARL observation on 24 Mar 2016 between 13:35 and 14:11 UTC. SSA and extinction coefficient are plotted at 880 nm (red) and at 532 (blue) obtained by Raman (lines) and Klett (dotted circles) methods.

differences at the same layer with an analogous relationship between both methods (Fig. 8).

536 0.92). The result lies within an appreciable consistency regarding uncertainty analysis
537 provided in Section 4, stating that conversion of the extinction coefficient at 880 nm results in
538 greater errors.

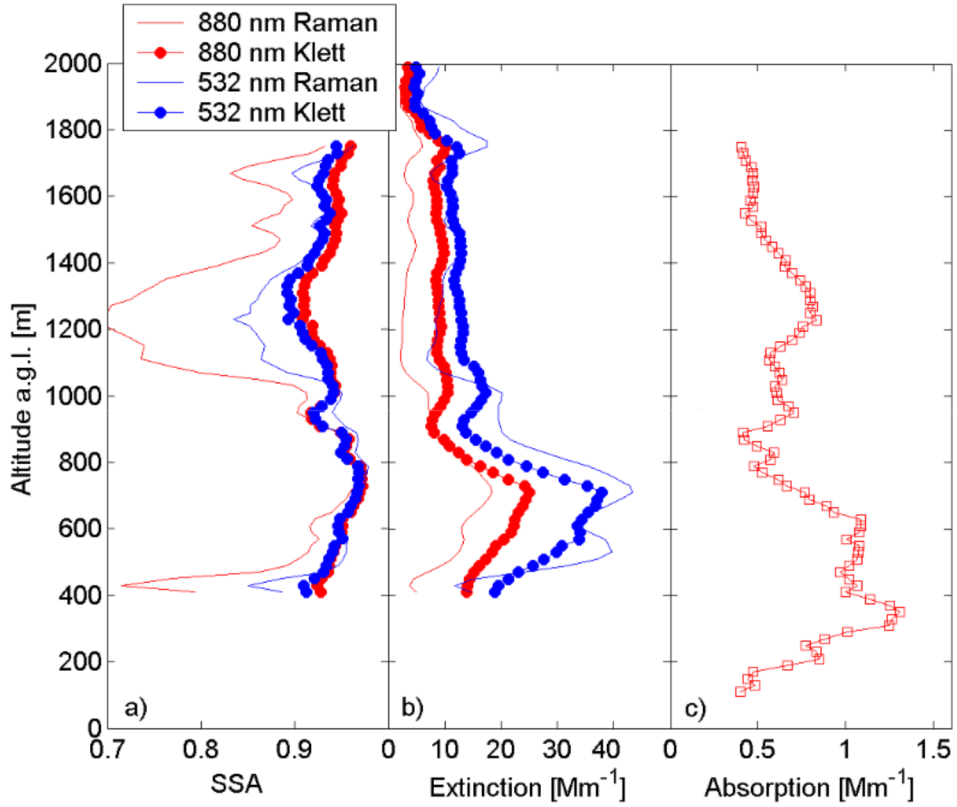

539

540 Fig. 8. Profiles of SSA (a), extinction coefficient (b), and absorption coefficient at 880 nm (c)
541 in Mm^{-1} obtained during the tethered balloon and KARL observation on 24 Mar 2016
542 between 17:26 and 18:01 UTC. The SSA and extinction coefficient are plotted at 880 nm
543 (red) and at 532 (blue) in the case of the Raman (lines) and Klett (dotted circles) methods.
544
545
546 Overall, we note a moderate agreement between low SSA and high EBC concentrations. The
547 relationship seems to be satisfied more around the 1.2-km layer in the first balloon profile
548 (blue, afternoon) and for the 400-m layer in the second profile (green, evening). The latter
549 was also measured by lidar, although 200 m higher, closer to 600 m a.g.l. The vertical
550 discrepancies might be related to the balloon drifting horizontally due to the wind in the

556 **5.2. Aerosol event between 7 and 8 April 2015.**

557 Between 7 and 8 April 2015 transport of anthropogenic particles was confirmed by the
558 NAAPS results (Fig. 9). The AOD around the northern part of Svalbard was between 0.1 and
559 0.2 at 550 nm. The region of relatively high anthropogenic sulphates AOD covers the area of
560 the North Pole (reddish colour in Fig. 9a, b). Biomass burning activity during this period was
561 very low, while dust aerosol was predicted far from Svalbard (Western Canada and Alaska
562 and Western Siberia). The Microtops II sun photometer observation in Ny-Ålesund shows the
563 AOD around 0.10-0.11 (500 nm) on 7 April and 0.07-0.09 during 8 April.

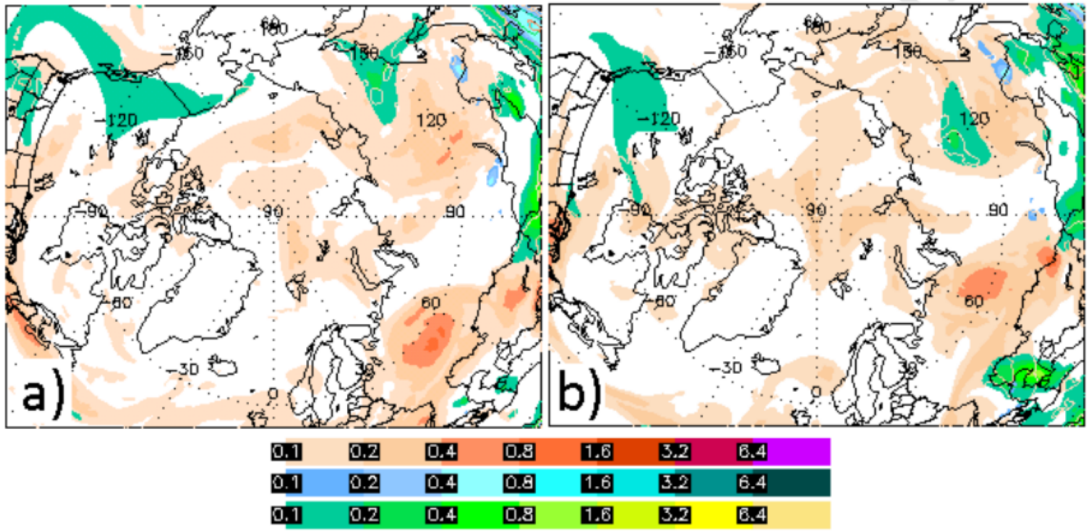

564

565 Fig. 9. NAAPS aerosol optical depth at 550 nm for 00 UTC on (a) 7 and (b) 8 April of
566 2015. The orange/red correspond to anthropogenic sulphates, blue to smoke particles, and
567 green/yellow to dust. The colour bars for each aerosol component vary between 0.1 and 12.8.
568

569 The 144-hour back trajectories ending in Ny-Ålesund at 12 UTC on 7 (a) and 8 (b) April 2015
570 show the transport of air mass from middle latitudes (mostly Eastern Europe). During the first
571 48 hours the transport at 1, 3, and 5 km is very similar through the Barents Sea and Northern
572 Scandinavia (Fig. 10). After that the back trajectories spread and the source region for the
573 mass over Svalbard at 1 km was Western Russia and Kazakhstan. In case of the air mass at 3
574 km the back trajectories originated from Western Russia close to the border with Ukraine.
575 The transport at 5 km was from the south-eastern part of Europe (7 April) and from

maximum EBC concentration (about 200 ng/m^3, Fig. 11c). During this event high scattering AE (1.8-2.0) and fine to coarse ratio of the particle number concentration (2000-4000) as well as the low effective radius (about 0.22 µm) indicate small particles and probably anthropogenic origin of the pollution. Reduction of wind speed on 7 and 8 April allows use of the tethered balloon for EBC measurements and low cloud contamination to make sun photometer and lidar observations. In addition, low wind speed (less than 2 m/s) indicates a negligible impact of the sea salt aerosol on surface aerosol properties. Two days previously (5 April) the high wind speed (above 10 m/s) coincides with an increase of effective radius, aerosol scattering, and a decrease of scattering AE.

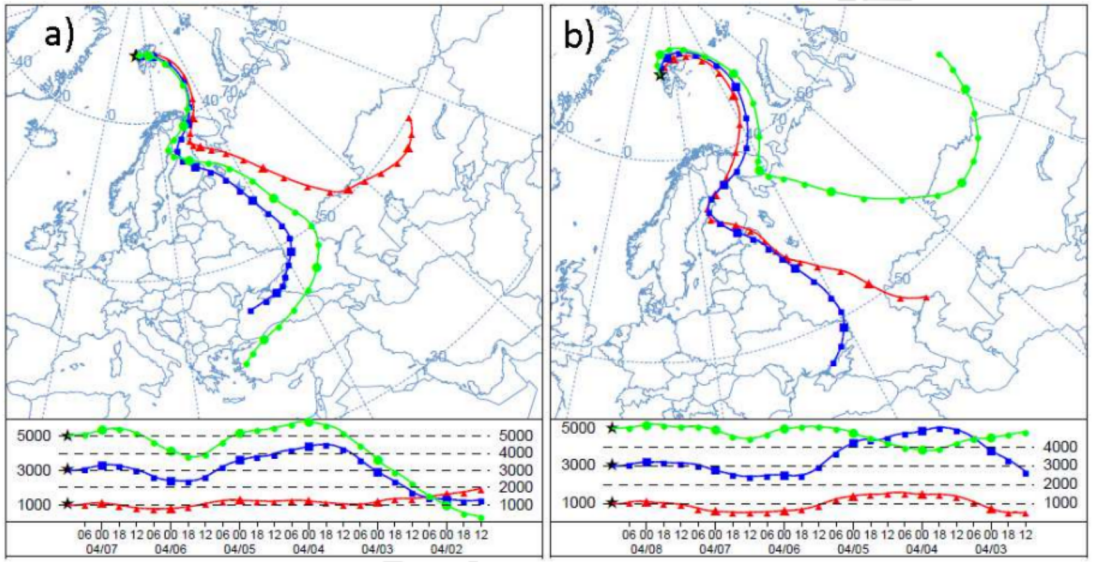

Fig. 10. 144-hour air mass back trajectories obtained from the NOAA HYSPLIT model at 12:00 UTC for (a) 7 and (b) 8 April 2016. Panels a-d are generated by means of the NCEP reanalysis database for Ny-Ålesund at 1, 3, and 5 km.

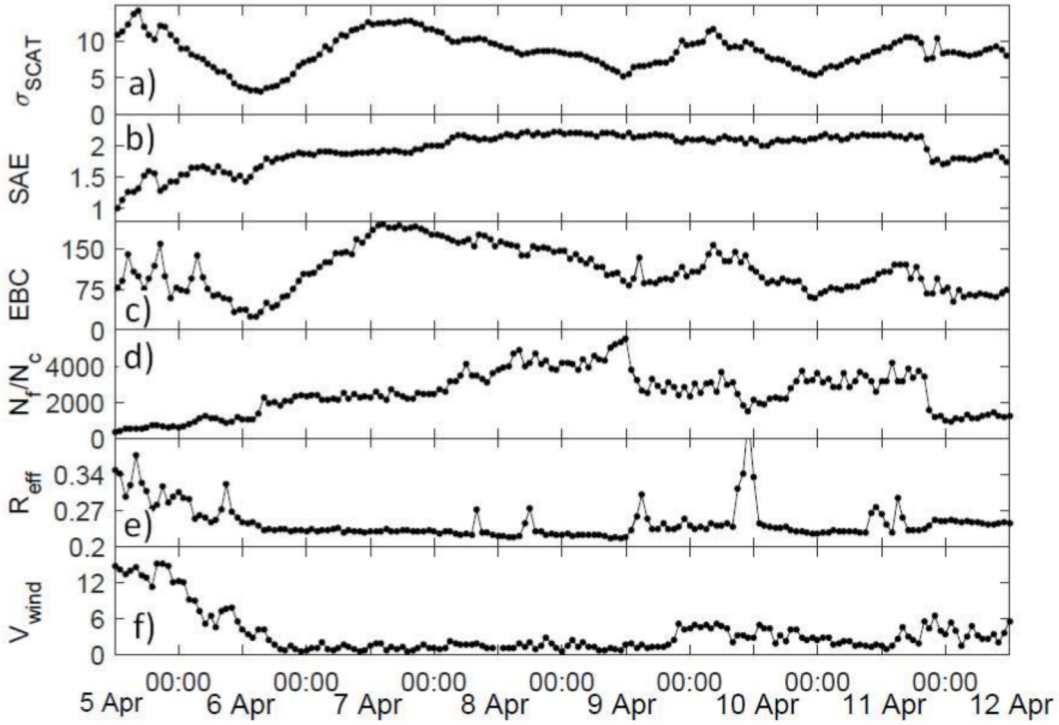

Fig. 11. Temporal variability of (a) aerosol scattering coefficient at 525 nm [Mm^{-1}], (b) scattering Angstrom exponent (SAE) both from TSI nephelometer, (c) EBC concentration at 880 nm [ng/m^3] from aethalometer AE-31, (d) fine to coarse particle number concentration, (e) effective radius [µm] both from Laser Aerosol Spectrometer 3340, and (f) wind speed [m/s] at Gruvebadet observatory between 5 and 11 April 2015.

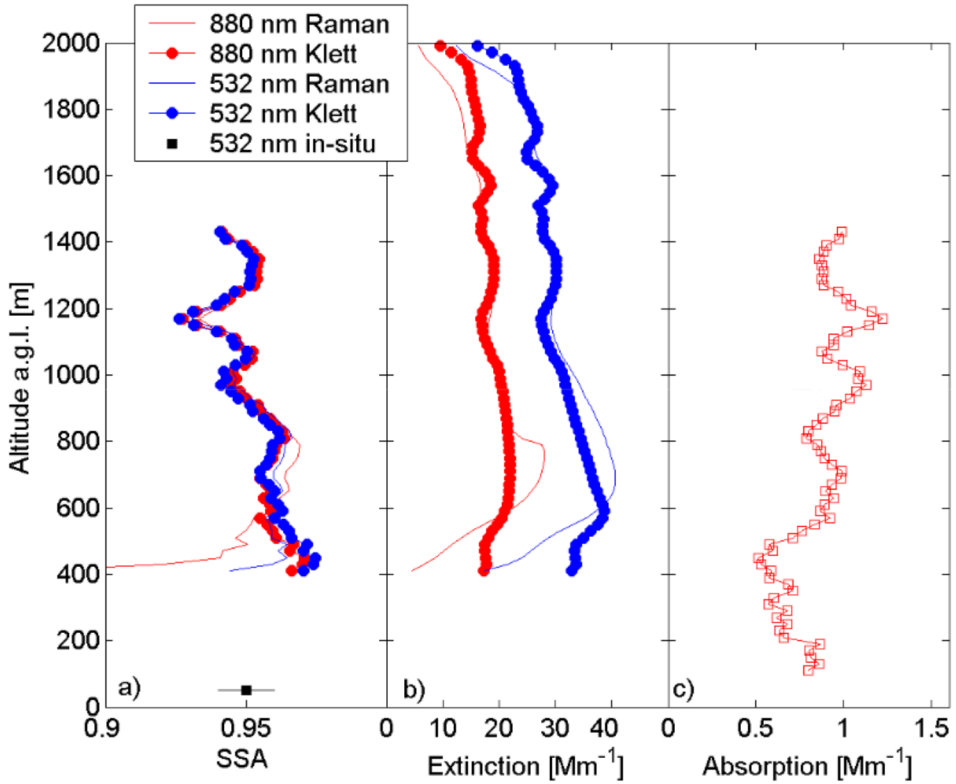

Fig. 12 Profiles of SSA (a), extinction coefficient (b), and absorption coefficient at 880 nm (c) in Mm^{-1} obtained during the tethered balloon and KARL observation on 7 April 2015 between 07:17 and 08:10 UTC. The SSA and extinction coefficient are plotted at 880 nm (red) and at 532 (blue) in case of the Raman (lines) and Klett (dotted circles) methods. The black square with error bar shows SSA at 532 nm measured by PAX in dry conditions.

Fig. 12 shows profiles of SSA (a), extinction (b), and absorption (c) coefficients retrieved from micro-aethalometer AE-51 and KARL lidar observation made between 07:17 and 08:10 UTC on 7 April 2015. All retrieved SSA profiles indicate similar vertical variability with a slightly decreasing trend from 0.97 at about 400 m to 0.94 at the level of 1400 m as a consequence of reduction of aerosol extinction and a weak enhancement of the absorption with altitude. Also, profiles performed between 11:23 and 12:03 UTC show similar negligible stratification, indicating a possible mixing condition within the lowermost

increases from a value close to zero at the surface to about 1 Mm^{-1} at 1400 m. In the case of the extinction coefficient retrieval, the difference between Raman and Klett methods is clearly visible.

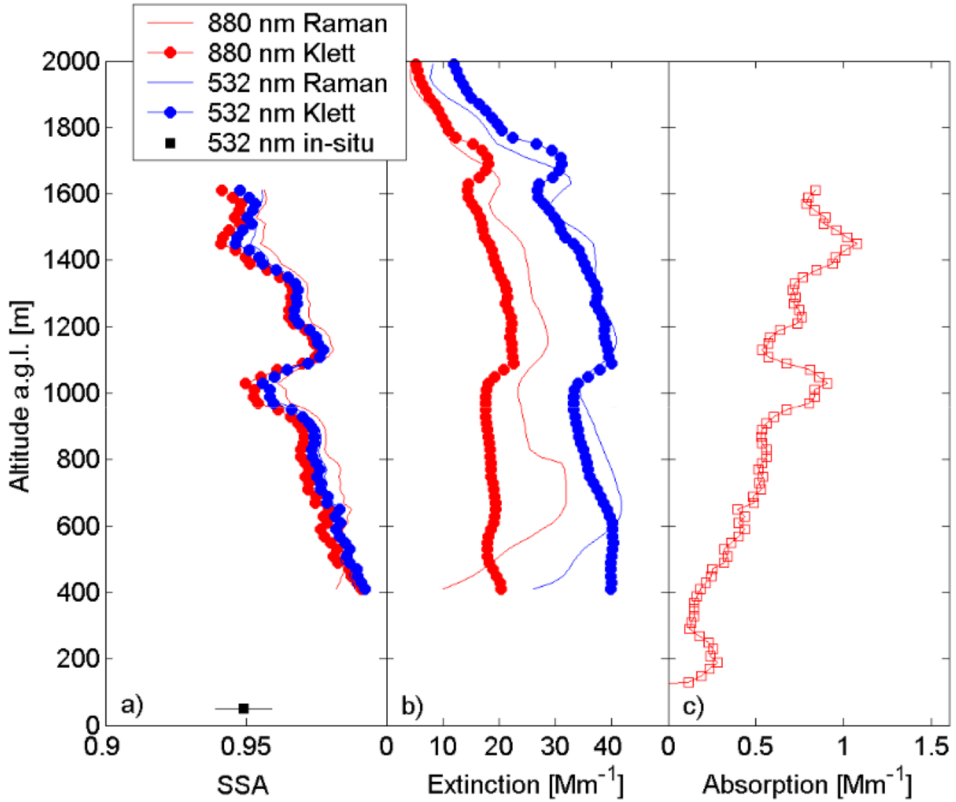

Fig. 13. Profiles of SSA (a), extinction (b) and absorption coefficients at 880 nm (c) in Mm^{-1} obtained during joint measurements by means of tethered balloon and KARL lidar on 7 April 2015 between 11:23 and 12:03 UTC. SSA and extinction coefficient are plotted at 880 nm (red) and at 532 nm (blue) in the case of the Raman (lines) and Klett (dotted circles) methods. The black square with error bar shows SSA at 532 nm measured by PAX in dry conditions.

Fig 14 presents profiles of single scattering properties obtained between 09:08 and 09:50 UTC on April 8. Vertical variability of SSA is small, and it declines with altitude from values 0.97-0.98 at 400 m to 0.91-0.92 at 1600 m. Some small difference between wavelength and methods (Fig. 14b) was found; however, it lies within the uncertainty range (see section

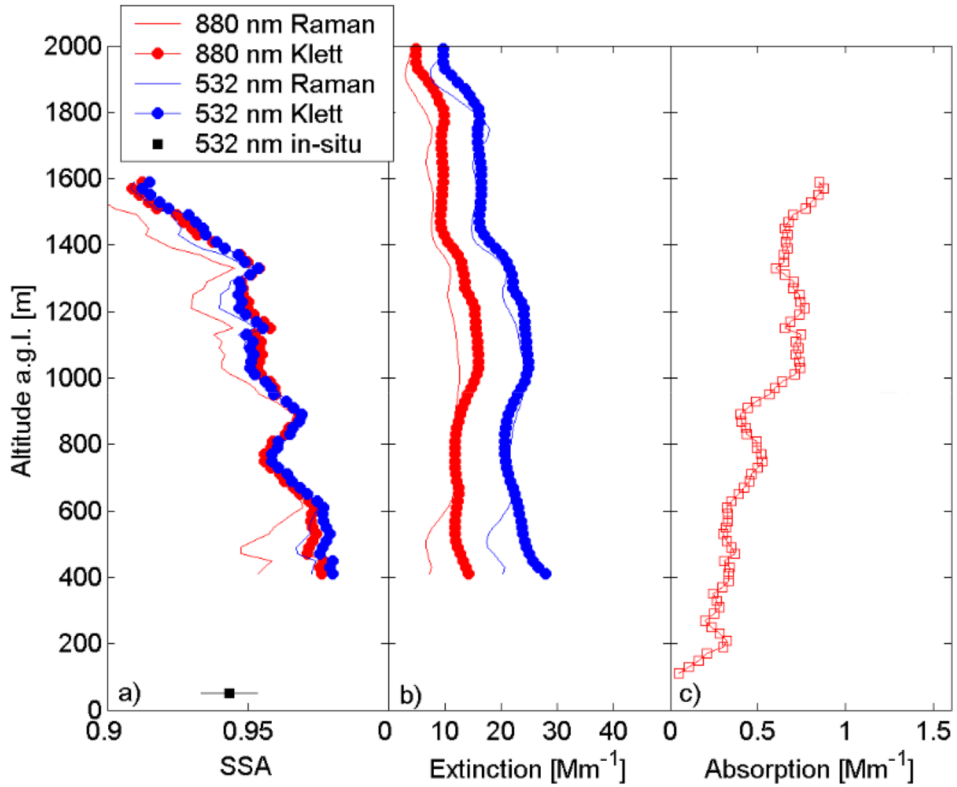

Fig. 14. Profiles of SSA (a), extinction (b), and absorption coefficients at 880 nm (c) in Mm^{-1} obtained during joint measurements by means of tethered balloon and KARL lidar on 8 April 2015 between 09:08 and 09:50 UTC. The SSA and extinction coefficient are plotted at 880 nm (red) and at 532 nm (blue) in the case of the Raman (lines) and Klett (dotted circles) methods. The black square with error bar shows SSA at 532 nm measured by PAX in dry conditions.

In all analysed cases from 2015 and 2016 the extinction and absorption coefficients are uncorrelated. This is not an artefact of the extinction retrieval in the because as it holds true also for the Klett method. Generally, SSA values are greater than 0.8, indicating that the absorbing aerosol component (EBC) is not correlated with sulphates and sea salt, considered the main Arctic aerosol species (Lisok et al., 2016). In addition, figures 12-14 show the surface SSA at 532 nm measured by PAX device. In all cases the surface values are lower in comparison to the SSA obtained from lidar and AE-51 at 400 m a.g.l. This is primarily due to

6. Profiles of EBC and total aerosol concentration

During the iAREA campaigns of 2015 and 2016 we performed measurements resulting in 93 tethered balloon profiles. Figure 15 shows single (grey lines) and mean (dots) profiles of EBC concentration (Fig. 15a), and total aerosol concentration (Fig. 15b) for particle diameters greater than 0.31 µm as well as the ratio of fine (0.31-0.51 µm) to total aerosol number concentration (Fig. 15c). The colours of the dots show the frequencies of the measurements at a given altitude. The mean profile reached up to 1.2 km (red colour). The mean profile of the EBC concentration slightly increases with altitude; aerosol concentration, however, indicates the opposite trend. Vertical variability of EBC and total aerosol concentration is small, regarding averaged profiles for spring season of 2015 and 2016. Furthermore, significant reduction of EBC concentration is observed above 1.6 km, but due to the small number of measurements at this altitude the results are rather uncertain. Although balloon profiling does not allow measurements of single scattering properties above 1.6 km to be conducted, if a long-range transport of EBC aerosol occurred it should have left a mark in the lidar data due to the hygroscopic properties of non-pure EBC particles. Also, in the lidar data for iAREA 2015 there was no hint of significant aerosol above 3 km. EBC concentrations close to the surface agree with observations performed by AE-31 (black square with error bar in Fig. 15a) at Gruvebadet (1 km distance from balloon launch site). The contribution of small particles (0.31-0.51 µm) to the number of particles larger than 0.51 µm is about 0.9. The mean values slightly increase with altitude due to reduction of the largest particles. Similar data were collected in 2016 (Fig. 16). Figures 16a and Fig. 16b show a flat profile with low values of EBC concentration and total aerosol concentration. In the case of EBC we observed its increasing profile up to 300 m and then almost constant concentration (about 100 ng/m^3) until 1.6 km. Similarly to 2015, a significant reduction of EBC concentration is observed above 1.6 km; however, its significance is doubtful regarding the low number of observations. Above 400 m a systematic reduction of particles in the profiles of the total number concentration is present. OPC-N2 (Fig. 16b) profiles seem to be noisier in comparison to the HandiLaz counter (Fig. 15b), which might be explained by different time resolution (1 second in OPC-N2 and 10 seconds in HandiLaz) but also by almost 10 times

696 underlining that this value is significantly larger than the standard effective radius due to the
697 fact that OPC-N2 does not measure particles below 0.38 µm diameter. Generally we found
698 some cases in 2016 where the average EBC concentration in the lowest 1 km was above 250
699 ng/m^3 and the aerosol concentration larger than 2.5 per cm^3 , which we did not find in the
700 spring of 2015.

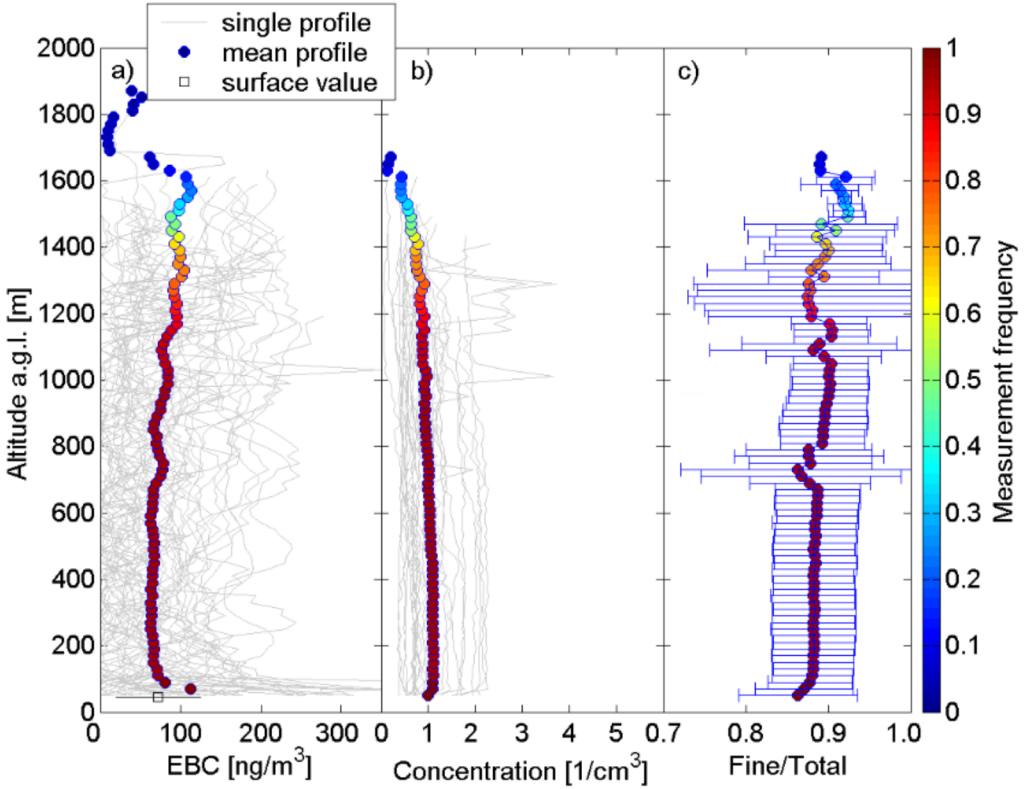

701

702 Fig. 15. Vertical variability of EBC concentration from AE-51(a), total aerosol concentration
703 (b), and fine (0.31-0.51 µm) to total particle number concentration (from 0.31 µm) by
704 HandiLaz averaged over 52 tethered balloon profiles conducted in March and April 2015.
705 Grey lines in (a) and (b) correspond to single profiles, while blue vertical lines (c) to standard
706 deviation. The averaged profiles are indicated by dots with the colour to show the frequency
707 of the measurements at different altitudes. Squared error bars in (a) present the EBC measured
708 at the surface by the AE-31 in Gruvebadet laboratory.

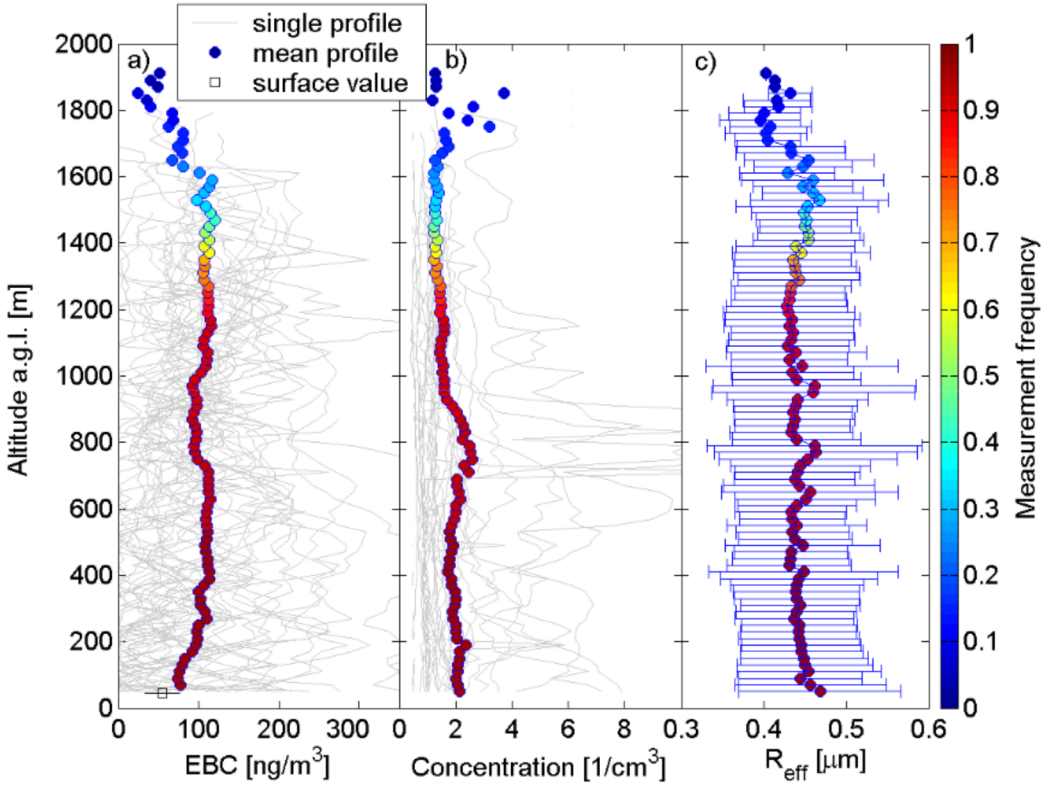

711

712 Fig. 16. Vertical variability of EBC concentration from AE-51(a), total aerosol concentration
713 (b), and effective radius for particles between 0.38 and 17 µm from OPC-N2 averaged over
714 41 tethered balloon profiles conducted in March and April 2016. Grey lines in (a) and (b)
715 correspond to single profiles, while blue vertical lines (c) to standard deviation. The averaged
716 profiles are indicated by dots, with the colour to show the frequency of the measurements at
717 different altitudes. Squared error bars in (a) present the EBC measured at the surface by the
718 AE-31 in Gruvebadet laboratory.

719

720 **7. Summary and conclusions**

721 In this study we summarised two years of joint measurements from lidar and tethered
722 balloons during the spring seasons 2015 and 2016. We found that mean profiles of EBC
723 concentration as well as aerosol number concentration are very uniform. In the case of aerosol

729 to Gruvebadet observatory. Although the AGAP payload was set up under a 50-m^3 helium
730 balloon, the gondola was heavy enough to be lifted only 1 km a.g.l. in moderate wind
731 conditions. A previous study of EBC and aerosol concentration profiles in Ny-Ålesund by
732 Ferrero et al. (2016) shows different vertical variability. During the spring seasons of 2011
733 and 2012, 15% of the profiles are homogenous, 17% and 48% of measurements indicate the
734 increase and decrease of aerosol concentration with altitude, respectively, while 20% are
735 defined as decoupled negative gradient profiles, characterised by negative gradients at
736 different altitudes depending on particle size. Summer profiles are more homogenous (37%)
737 and are effected by ship emissions. The PAM-ARCMIP (Polar Airborne Measurements and
738 Arctic Regional Climate Model Simulation Project) (Stone et al., 2010) and HIPPO (HIAPER
739 Pole-to-Pole Observations) (Schwarz et al., 2010) spring campaigns showed high EBC
740 concentrations close to the ground but also at high altitudes over the Arctic (Wofsy et al.,
741 2011). The HIPPO campaign revealed that in the lower troposphere the BC vertical gradient
742 can change seasonally from positive to negative (Schwarz et al., 2013). In this respect,
743 Spackman et al., 2010 and Koch et al., 2009 reported BC located mainly in the Arctic free
744 troposphere with a positive gradient in the lower troposphere.

745 In all analysed cases from 2015 and 2016 the extinction and absorption coefficient are
746 uncorrelated. A similar relation was reported by Lisok et al., 2016 for spring 2014 based on
747 the in-situ data obtained in Ny-Ålesund. Chemical data show that the increase of aerosol
748 extinction at the surface is usually due to sea-salt and sulphate particles advections, which do
749 not absorb the radiation in the visible range. Therefore, both optical parameters are not
750 correlated. In addition, the very small vertical variability of EBC and aerosol number
751 concentration up to 1.6 km is a consequence of the lack of significant aerosol event related to
752 the long-range transport from middle latitudes. Sea-salt events are usually observed in the first
753 few hundred metres, when high wind speed conditions with low clouds exist. Unfortunately,
754 such weather precluded balloon profiling due to the risk of losing equipment. Therefore, we
755 do not have data for sea-salt events. Also, Ferrero et al., 2016 showed negative correlations of
756 aerosol number and EBC concentration in a significant part of their spring profiles.

757 We found that synergy of lidar measurements with tethered balloon sounding provides

763 completely a different design of the AE-51 device. In addition, the most important part of
764 SSA error comes from spectral conversion of the absorption or extinction coefficient. To
765 avoid this, the new AE-52 micro-aethalometer can be used. This device includes two optical
766 channels (880 and 370 nm). The second channel is close to lidar 355 nm and 387 nm
767 detectors, so it allows retrieval of SSA in the UV range with less uncertainty. It can be useful
768 for organic carbon study with respect to biomass burning events. In the case of the
769 aethalometers (AE-31, AE-51), we have to remove the effect of the multiple scattering
770 between the filter and the aerosol deposited on it. Generally, this problem is very complicated
771 because the correction depends not only on the aerosol scattering but also on the aerosol
772 absorption that would be retrieved. In this study we estimated the multiple scattering factor
773 based on the comparison with photo-acoustic PAX instruments (532 nm, 870 nm). The total
774 SSA uncertainty from the lidar and AE-51 micro-aethalometer measurements is about ±0.01,
775 ±0.025, and ±0.04, respectively, for SSA 0.98, 0.95, and 0.90 between 500 and 1000 m. In the
776 upper layer the SSA error increases slightly above 1500 m, where the absorption coefficient is
777 relatively smaller. The retrieved SSA profiles show usually very similar vertical variability in
778 case of the Raman and Klett's methods and for both 532 and 880 nm wavelengths. However,
779 in a few cases the values of SSA are different at certain altitudes. The lowest SSA has been
780 found for the Raman method at the altitudes where the extinction coefficient is very low. For
781 most of the data the SSA variability with altitude is rather small, especially between 7 and 8
782 April 2015. We found that the Klett approach is slightly more appropriate for SSA estimation
783 in Arctic conditions. In general, it depends on the lidar system, light, and aerosol conditions.
784 During night and stable aerosol conditions the Raman method is better. The Klett method
785 requires the AOD observations, which are usually available only during the daytime. We
786 recommended using the Klett approach during the day and during dynamic changes in the
787 aerosol conditions. In this case the Raman method requires long time averaging (about 1-2
788 hour or longer) of lidar signal while vertical profiling by tethered balloon or UAV is much
789 faster. Therefore, during such conditions (e.g. rapid change of the PBL height) the Klett
790 method with short averaging should be used. Our method for estimation of the vertical
791 profiles of SSA is more appropriate for polluted regions, where the EBC concentration is

UAV (Chilinski et al., 2016) can be used to estimate profiles of EBC and aerosol absorption coefficient, and additional lidar or ceilometer observation to obtain the SSA profiles.

Acknowledgements

The authors would like to acknowledge the support for this research from the Polish-Norwegian Research Programme operated by the National Centre for Research and Development under the Norwegian Financial Mechanism 2009-2014 in the frame of Project Contract No Pol-Nor/196911/38/2013 and also project KNOW, Leading National Research Centre received by the Centre for Polar Studies for the period 2014-2018 established by regulation No. 152 (2013, Nov 14) of the Rector of the University of Silesia.

References

Alexandrov, M.D., A. Marshak, B. Cairns, A.A. Lacis, and B.E. Carlson, 2004: Automated cloud screening algorithm for MFRSR data. *Geophys. Res. Lett.*, 31, L04118, doi:10.1029/2003GL019105.

Anderson, T. L., Covert, D. S., Marshall, S. F., Laucks, M. L., Charlson, R. J., Waggoner, A. P., Ogren, J. A., Caldow, R., Holm, R. L., Quant, F. R., Sem, G. J., Wiedensohler, A., Ahlquist, N. A., and Bates, T. S., (1996). Performance characteristics of a high-sensitivity, three-wavelength, total scatter/backscatter nephelometer, J. Atmos. Oceanic Technol., 13, 967–986.

Anderson, T. L. and Ogren, J. A. (1998), Determining aerosol radiative properties using the TSI 3563 integrating nephelometer, Aerosol Sci. Tech., 29, 57–69.

Ansmann, A., Wandinger, U., Riebesell, M., Weitcamp, C., Michaelis, W. (1992), Independent measurement of extinction and backscatter profiles in cirrus clouds by using a combined Raman elastic-backscatter lidar, Applied Opt., 31/33, 7113 - 7131, doi: 10.1364/AO.31.007113.

Bond, T. C., S. Doherty, D. Fahey, P. M. Forster, T. Berntsen, B. J. DeAngelo, M. G. Flanner, S. Ghan, B. Kärcher, D. Koch, S. Kinne, Y. Kondo, P. K. Quinn, M. C. Sarofim, M. G. Schultz, M. Schulz, C. Venkataraman, H. Zhang, S. Zhang, N. Bellouin, S. K. Guttikunda,

830 Chaikovsky, A., Dubovik, O., Holben, B., Bril, A., Goloub, P., Tanré, D., Pappalardo, G.,
831 Wandinger, U., Chaikovskaya, L., Denisov, S., Grudo, J., Lopatin, A., Karol, Y.,
832 Lapyonok, T., Amiridis, V., Ansmann, A., Apituley, A., Allados-Arboledas, L.,
833 Binietoglou, I., Boselli, A., D'Amico, G., Freudenthaler, V., Giles, D., Granados-Muñoz,
834 M. J., Kokkalis, P., Nicolae, D., Oshchepkov, S., Papayannis, A., Perrone, M. R.,
835 Pietruczuk, A., Rocadenbosch, F., Sicard, M., Slutsker, I., Talianu, C., De Tomasi, F.,
836 Tsekeri, A., Wagner, J., and Wang, X.: Lidar-Radiometer Inversion Code (LIRIC) for the
837 retrieval of vertical aerosol properties from combined lidar/radiometer data: development
838 and distribution in EARLINET, Atmos. Meas. Tech., 9, 1181-1205, doi:10.5194/amt-9-
839 1181-2016, 2016.

840 Chilinski, M.T., K.M. Markowicz, and J. Markowicz, 2016, Observation of vertical variability
841 of black carbon concentration in lower troposphere on campaigns in Poland, Atmos.
842 Environ., 137, 155–170.

843 Collaud-Coen, M., Weingartner, E., Apituley, A., Ceburnis, D., Fierz-Schmidhauser, R.,
844 Flentje, H., Henzing, J. S., Jennings, S. G., Moerman, M., Petzold, A., Schmid, O., and
845 Baltensperger, U.: Minimizing light absorption measurement artifacts of the Aethalometer:
846 evaluation of five correction algorithms, Atmos. Meas. Tech., 3, 457–474,
847 doi:10.5194/amt-3-457-2010, 2010.

848 Chaikovsky, A., Dubovik, O., Holben, B., Bril, A., Goloub, P., Tanré, D., Pappalardo, G.,
849 Wandinger, U., Chaikovskaya, L., Denisov, S., Grudo, J., Lopatin, A., Karol, Y.,
850 Lapyonok, T., Amiridis, V., Ansmann, A., Apituley, A., Allados-Arboledas, L.,
851 Binietoglou, I., Boselli, A., D'Amico, G., Freudenthaler, V., Giles, D., Granados-Muñoz,
852 M. J., Kokkalis, P., Nicolae, D., Oshchepkov, S., Papayannis, A., Perrone, M. R.,
853 Pietruczuk, A., Rocadenbosch, F., Sicard, M., Slutsker, I., Talianu, C., De Tomasi, F.,
854 Tsekeri, A., Wagner, J., and Wang, X. (2016), Lidar-Radiometer Inversion Code (LIRIC)
855 for the retrieval of vertical aerosol properties from combined lidar/radiometer data:
856 development and distribution in EARLINET, Atmos. Meas. Tech., 9, 1181-1205,
857 doi:10.5194/amt-9-1181-2016.

858 Draxler, R. R., Rolph, G. D., 2010, HYSPLIT (HYbrid Single-Particle Lagrangian Integrated

862 Dubovik, O., Holben, B., Eck, T.F., Smirnov, A., Kaufman, Y.J., King, M.D., Tanré, D., & I.
863 Slutsker, I. (2002). Variability of absorption and optical properties of key aerosol types
864 observed in worldwide locations. *Journal of the Atmospheric Sciences, 59*, 590–608.
865 Eleftheriadis, K., Vratolis, S., and Nyeki, S. (2009), Aerosol black carbon in the European
866 Arctic: Measurements at Zeppelin station, Ny-Ålesund, Svalbard from 1998–2007,
867 Geophys. Res. Lett., 36, L02809, doi:10.1029/2008GL035741. Fernandes, K., W.
868 Baethgen, S. Bernardes, R. DeFries, D. G. DeWitt, L. Goddard, W. Lavado, D. E. Lee, C.
869 Padoch, M. Pinedo-Vasquez, and M. Uriarte (2011), North tropical Atlantic influence on
870 western Amazon fire season variability, Geophys. Res. Lett., 38, L12701,
871 doi:10.1029/2011GL047392.
872 Ferrero, L., Cappelletti, D., Busetto, M., Mazzola, M., Lupi, A., Lanconelli, C., Becagli, S.,
873 Traversi, R., Caiazzo, L., Giardi, F., Moroni, B., Crocchianti, S., Fierz, M., Močnik, G.,
874 Sangiorgi, G., Perrone, M. G., Maturilli, M., Vitale, V., Udisti, R., and Bolzacchini, E.:
875 Vertical profiles of aerosol and black carbon in the Arctic: a seasonal phenomenology
876 along 2 years (2011–2012) of field campaigns, Atmos. Chem. Phys., 16, 12601-12629,
877 doi:10.5194/acp-16-12601-2016, 2016.
878 Ferrero, L., Mocnik, G., Ferrini, B. S., Perrone, M. G., Sangiorgi, G. and Bolzacchini, E.
879 (2011), Vertical profiles of aerosol absorption coefficient from micro-Aethalometer data
880 and Mie calculation over Milan., Sci. Total Environ., 15 409(14), 2824–37,
881 doi:10.1016/j.scitotenv.2011.04.022.
882 Hansen, J., Mki. Sato, R. Ruedy, (2005), Efficacy of climate forcings, J. Geophys. Res., 110,
883 D18104, doi:10.1029/2005JD005776.
884 Haywood, J.M., and V. Ramaswamy (1998), Global sensitivity studies of the direct radiative
885 forcing due to anthropogenic sulfate and black carbon aerosols, Journal of Geophysical
886 Research 103: doi: 10.1029/97JD03426. issn: 0148-0227.
887 Heintzenberg, J., Wiedensohler, A., Tuch, T. M., Covert, D. S., Sheridan, P., Ogren, J. A.,
888 Gras, J., Nessler, R., Kleefeld, C., Kalivitis, N., Aaltonen, V., Wilhelm, R.-T. and
889 Havlicek, M. 2006. Intercomparisons and Aerosol Calibrations of 12 Commercial
890 Integrating Nephelometers of Three Manufacturers. *J. Atmos. Ocean. Tech.*, 23: 902–914.

895 Hoffmann, A. (2011), Comparative aerosol studies based on multi-wavelength Raman LIDAR
896 at Ny Ålesund, Spitsbergen, PhD Thesis Uni. Potsdam,
897 http://epic.awi.de/29932/1/Hof2011g.pdf.
898 Holben, B.N., T.F. Eck, I. Slutsker, D. Tanré, J.P. Buis, A. Setzer, E.F. Vermote, J.A. Reagan,
899 Y.J. Kaufman, T. Nakajima, F. Lavenu, I. Jankowiak, and A. Smirnov (1998), AERONET
900 – A federated instrument network and data archive for aerosol characterization, Remote
901 Sensing of Environment, 66, 1: 1-16.
902 Johnson, B. T., B. Heese, S. A. McFarlane, P. Chazette, A. Jones, and N. Bellouin (2008),
903 Vertical distribution and radiative effects of mineral dust and biomass burning aerosol over
904 West Africa during DABEX, J. Geophys. Res., 113, D00C12, doi:10.1029/2008JD009848.
905 Jin, Y. K., K. Kai, T. Kawai, T. Nagai, A. Sakai, A. Yamazaki, D. Uchiyama, N. Batdorj,
906 Sugimoto, and T. Nishizawa (2015), Ceilometer calibration for retrieval of aerosol optical
907 properties, Journal of Quantitative Spectroscopy and Radiative Transfer, 153, pages 49-56.
908 Kaskaoutis, D. G., Kambezidis, H. D., Hatzianastassiou, N., Kosmopoulos, P. G., and
909 Badarinath, K. V. S., (2007), Aerosol climatology: dependence of the Angstrom exponent
910 on wavelength over four AERONET sites, Atmos. Chem. Phys. Discuss., 7, 7347-7397,
911 doi:10.5194/acpd-7-7347-2007.
912 Klett, J.D. (1981), stable analytical inversion solution for processing lidar returns. Appl. Opt.
913 20,2, 211 – 220, doi: 10.1364/AO.20.000211.
914 Koch, D., *and* A. D. Del Genio (*2010*), Black carbon semi‐direct effects on cloud cover:
915 Review and synthesis, Atmos. Chem. Phys., 10, 7685–7696.
916 Kok, G., Walker, J.W., Arnott, W.P., Arnold, I.J., Keady, P.B., (2010), Photoacoustic
917 Extinctiometer (PAX): a New Instrument for Measurement of Climateerelevant Optical
918 Properties of Aerosols. American Association for Aerosol Research, Oregon Convention,
919 Portland, Oregon, USA.
920 Kolgotin, A. and Müller, D. (2008), Theory of inversion with twodimensional regularization:
921 profiles of microphysical particie properties derived from multiwavelength lidar
922 measurements, Appl. Opt., 47, 4472–4490.
923 Lisok, J., K.M. Markowicz, C. Ritter, R. Neuber, P. Makuch, P. Pakszys, P. Markuszewski,

928 Markowicz, K. M., T. Zielinski, S. Blindheim, M. Gausa, A.K. Jagodnicka, A.E. Kardas, W.
929 Kumala, Sz.P. Malinowski, M. Posyniak, T. Petelski, T. Stacewicz (2012), Study of
930 vertical structure of aerosol optical properties by sun photometers and ceilometer during
931 macron campaign in 2007, Acta Geophys., 60(5), 1308-1337, doi: 10.2478/s11600-011-
932 0056-7.
933 Marlon, J. R., P. J. Bartlein, C. Carcaillet, D. G. Gavin, S. P. Harrison, P. E. Higuera, F. Joos,
934 M. J. Power, and I. C. Prentice (2008), Climate and human influences on global BB over
935 the past two millennia, Nature Geosci., 1, 697–702, doi:10.1038/ngeo313.
936 Massoli, P., D.M. Murphy, D.A. Lack, T. Baynard, C.A. Brock, E.R. Lovejoy, (2009),
937 Uncertainty in Light Scattering Measurements by TSI Nephelometer: Results from
938 Laboratory Studies and Implications for Ambient Measurements, Aerosol Science and
939 Technology, 43:1064-1074.
940 Mazzola, M., M. Busetto, L. Ferrero, A. P. Viola, and D. Cappelletti, (2016), AGAP: an
941 atmospheric gondola for aerosol profiling, Rend. Fis. Acc. Lincei (2016) 27 (Suppl
942 1):S105–S113, DOI 10.1007/s12210-016-0514-x.
943 Morys, M., F. M. III. Mims, S. Hagerup (2001), Design, calibration, and performance of
944 MICROTOPS II handheld ozone monitor and Sun photometer, J. Geophys. Res.:
945 Atmospheres, 106, 14573.
946 Müller, D., Wandinger, U., and Ansmann, A. (1999), Microphysical particle parameters from
947 extinction and backscatter lidar data by inversion with regularization: theory, Appl. Opt.
948 38, 2346–2357.
949 Myhre, G., B. H. Samset, M. Schulz, Y. Balkanski, S. Bauer, T. K. Berntsen, H. Bian, N.
950 Bellouin, M. Chin, T. Diehl, R. C. Easter, J. Feichter, S. J. Ghan, D. Hauglustaine, T.
951 Iversen, S. Kinne, A. Kirkevåg, J.-F. Lamarque, G. Lin, X. Liu, M. T. Lund, G. Luo,
952 X. Ma, T. van Noije, J. E. Penner, P. J. Rasch, A. Ruiz, Ø. Seland, R. B. Skeie, P.
953 Stier, T. Takemura, K. Tsigaridis, P. Wang, Z. Wang, L. Xu, H. Yu, F. Yu, J.-H.
954 Yoon, K. Zhang, H. Zhang, and C. Zhou (2013), Radiative forcing of the direct aerosol
955 effect from AeroCom Phase II simulations, Atmos. Chem. Phys., 13, 1853-1877,
956 doi:10.5194/acp-13-1853-2013.

962 Pakszys P., T. Zielinski, K. Markowicz, T. Petelski, P. Makuch, J. Lisok, M. Chilinski, A.
963 Rozwadowska, Ch. Ritter, R. Neuber, R. Udisti, M. Mazzola (2015), Annual changes of
964 aerosol optical depth and Ångström exponent over Spitsbergen, Springer Series:
965 GeoPlanet: Earth and Planetary Sciences; ISBN 978-3-319-14282-1, pp. 23-37.
966 Petzold, A., J. A. Ogren, M. Fiebig, P. Laj, S. M. Li, U. Baltensperger, T. Holzer-Popp, S.
967 Kinne, G. Pappalardo, N. Sugimoto, C. Wehrli, A. Wiedensohler, and X.Y. Zhang (2013),
968 Recommendations for reporting "black carbon" measurements, Atmos. Chem. Phys., 13,
969 8365-8379.
970 Ramana, M. V., Ramanathan, V., Kim, D., Roberts, G. C. and Corrigan, C. E. (2007), Albedo,
971 atmospheric solar absorption and heating rate measurements with stacked UAVs. Q.J.R.
972 Meteorol. Soc., 133: 1913–1931. doi:10.1002/qj.172.
973 Ramanathan, V., P. J. Crutzen, J. T. Kiehl, and D. Rosenfeld, (2001), Aerosols, climate, and
974 the hydrological cycle. *Science,* 294**,** 2119-2124.
975 Ramanathan, V., Carmichael, G. (2008), Global and regional climate changes due to black
976 carbon, Nat. Geosci., 1, 221-227.
977 Ramanathan V., M.V. Ramana, G. Roberts, D. Kim, C.E. Corrigan, C.E. Chung & D. Winker
978 (2007), Warming trends in Asia amplified by brown cloud solar absorption. Nature, 448,
979 575-578 doi:10.1038/nature06019.Ran, L., Deng, Z., Xu, X., Yan, P., Lin, W., Wang, Y.,
980 Tian, P., Wang, P., Pan, W., and Lu, D. (2016), Vertical profiles of black carbon measured
981 by a micro-aethalometer in summer in the North China Plain, Atmos. Chem. Phys., 16,
982 10441-10454, doi:10.5194/acp-16-10441-2016.
983 Ritter, C., R. Neuber, K.M. Markowicz, I.S. Stachlewska, M. Chilinski, J. Lisok, P. Makuch,
984 P. Pakszys, P. Markuszewski, A. Rozwadowska, T. Petelski, T. Zielinski, S. Becagli, R.
985 Traversi, R. Udisti, M. Gausa (2016), Raman-lidar derived aerosol properties over Ny-
986 Ålesund, Spitsbergen during the Arctic Haze season 2014, *Atmospheric Environment* 141,
987 1-19.
988 Rizzo, L. V., Correia, A. L., Artaxo, P., Procópio, A. S., and Andreae, M. O. (2011), Spectral
989 dependence of aerosol light absorption over the Amazon Basin, Atmos. Chem. Phys., 11,
990 8899-8912, doi:10.5194/acp-11-8899-2011.

995 Samset, B. H., Myhre, G., Schulz, M., Balkanski, Y., Bauer, S., Berntsen, T. K., Bian, H.,
996 Bellouin, N., Diehl, T., Easter, R. C., Ghan, S. J., Iversen, T., Kinne, S., Kirkevåg, A.,
997 Lamarque, J.-F., Lin, G., Liu, X., Penner, J. E., Seland, Ø., Skeie, R. B., Stier, P.,
998 Takemura, T., Tsigaridis, K., and Zhang, K.: Black carbon vertical profiles strongly affect
999 its radiative forcing uncertainty, Atmos. Chem. Phys., 13, 2423-2434, doi:10.5194/acp-13-
1000 2423-2013, 2013.
1001 Schmid, O., Artaxo, P., Arnott, W. P., Chand, D., Gatti, L. V., Frank, G. P., Hoffer, A.,
1002 Schnaiter, M., and Andreae, M. O.: Spectral light absorption by ambient aerosols
1003 influenced by biomass burning in the Amazon Basin. I: Comparison and field calibration
1004 of absorption measurement techniques, Atmos. Chem. Phys., 6, 3443–3462,
1005 doi:10.5194/acp-6-3443-2006, 2006.
1006 Schuster, G. L., Dubovik, O., Arola, A., Eck, T. F., and Holben, B. N.: Remote sensing of
1007 soot carbon – Part 2: Understanding the absorption Ångström exponent, Atmos. Chem.
1008 Phys., 16, 1587-1602, doi:10.5194/acp-16-1587-2016, 2016.
1009 Schwarz, J. P., Samset, B. H., Perring, A. E., Spackman, J. R., Gao, R. S., Stier, P., Schultz,
1010 M. G., Moore, F. L., Ray, E. A., and Fahey, D. W.(2013), Global-scale seasonally resolved
1011 black carbon vertical profiles over the Pacific, Geophys. Res. Lett., 40, 5542–5547.
1012 Segura, S., Estellés, V., Titos, G., Lyamani, H., Utrillas, M. P., Zotter, P., Prévôt, A. S. H.,
1013 Močnik, G., Alados-Arboledas, L., and Martínez-Lozano, J. A.: Determination and
1014 analysis of in situ spectral aerosol optical properties by a multi-instrumental approach,
1015 Atmos. Meas. Tech., 7, 2373-2387, doi:10.5194/amt-7-2373-2014, 2014.
1016 Seinfeld, J.(2008), Black carbon and brown clouds, Nature Geosci., 1, 15–16.
1017 Smimov, A., Holben, B.N., Eck, T.F., Dubovik, O., (2000), Cloud-Screening and quality
1018 control algorithms for the AERONET database. Remote Sens. Environ. 73, 337e349.
1019 Soni, K., S. Singh, T. Bano, R. S. Tanwar, S. Nath, (2011), Wavelength Dependence of the
1020 Aerosol Angstrom Exponent and Its Implications Over Delhi, India, Aerosol Science and
1021 Technology, 45 (12), 1488-1498.
1022 Spackman, J. R., Gao, R. S., Neff, W. D., Schwarz, J. P., Watts, L.A., Fahey, D. W.,
1023 Holloway, J. S., Ryerson, T. B., Peischl, J., and Brock, C. A.(2010), Aircraft observations

1028 Stone, R. S., Herber, A., Vitale, V., Mazzola, M., Lupi, A., Schnell, R. C., Dutton, E. G., Liu,
1029 P. S. K., Li, S. M., Dethloff, K., Lampert, A., Ritter, C., Stock, M., Neuber, R., and
1030 Maturilli, M.(2010), A three-dimensional characterization of Arctic aerosols from airborne
1031 Sun photometer observations: PAMARCMIP, J. Geophys.Res.-Atmos., 115, D13203,
1032 doi:10.1029/2009jd013605.
1033 The Fourth Assessment Report of the IPCC, (2007). The Fifth Assessment Report of the
1034 IPCC, (2013).
1035 Toledano, C. , Cachorro, V. , Gausa, M. , Stebel, K. , Aaltonen, V. , Berjon, A. , Ortis, J. P. ,
1036 de Frutos, A. M. , Bennouna, Y. , Blindheim, S. , Myhre, C. L. , Zibordi, G. , Wehrli, C. ,
1037 Kratzer, S. , Hakanson, B. , Carlund, T. , de Leuww, G. and Herber, A. (2012), Overview
1038 of Sun photometer measurements of aerosol properties in Scandinavia and Svalbard ,
1039 Atmospheric Environment., 52 , pp. 18-28 . doi: 10.1016/j.atmosenv.2011.10.022
1040 Veselovskii, I., Kolgotin, A., Griaznov, V., Muuller, D., Wandinger, U., and Whiteman, D.
1041 (2002), Inversion with regularization for the retrieval of tropospheric aerosol parameters
1042 from multi-wavelength lidar sounding, Appl. Opt., 41, 3685–3699..
1043 Veselovskii, I., Kolgotin, A., Griaznov, V., Muller, D., Franke, K., and Whiteman, D. N.
1044 (2004), Inversion of multi-wavelength Raman lidar data for retrieval of bimodal aerosol
1045 size distribution, Appl. Opt., 43, 1180–1195, 2004.
1046 Virkkula, A., Chi, X., Ding, A., Shen, Y., Nie, W., Qi, X., Zheng, L., Huang, X., Xie, Y.,
1047 Wang, J., Petäjä, T., and Kulmala, M. (2015), On the interpretation of the loading
1048 correction of the aethalometer, Atmos. Meas. Tech., 8, 4415-4427, doi:10.5194/amt-8-
1049 4415-2015.
1050 Wang, S.-H., N.-H. Lin, M.-D. Chou, and J.-H. Woo (2007), Estimate of radiative forcing of
1051 Asian biomass-burning aerosols during the period of TRACE-P, J. Geophys. Res., 112,
1052 D10222, doi:10.1029/2006JD007564.
1053 Wofsy, S. C., the HIPPO Science Team and Cooperating Modellers and Satellite Teams,
1054 (2011), HIAPER Pole-to-Pole Observations (HIPPO): fine grained, global-scale
1055 measurements of climatically important atmospheric gases and aerosols, Philos. T. R.Soc.,
1056 369, 2073–2086.

1060 Zarzycki, C. M. and Bond, T. C. (2010), How much can the vertical distribution of black
1061 carbon affect its global direct radiative forcing?, Geophys Res Lett, 37, L20807,
1062 doi:10.1029/2010gl044555.
1063 Zawadzka, O., M. Posyniak, K. Nelken, P. Markuszewski, M. T. Chiliński, D. Czyżewska,
1064 J. Lisok, K. M. Markowicz, 2017, Study of the vertical variability of the aerosol
1065 properties based on cable cars in-situ measurements, Atmospheric Pollution Research,
1066 in press.

Highlights

- a new methodology to retrieve profiles of single-scattering albedo
- reasonable agreement between Raman and Klett retrievals
- small variability of single-scattering albedo with altitude over Svalbard
- slight increase in mean equivalent black carbon concentration with altitude